THE JOURNAL OF CHEMICAL PHYSICS **122**, 224321 (2005)

Radiative association of He^+ with H_2 at temperatures below 100 K

Felicja Mrugała[a]
Institute of Physics, Nicolaus Copernicus University, Grudziadzka 5, PL 87-100 Torun, Poland

Wolfgang P. Kraemer
Max-Planck-Institute of Astrophysics, Postfach 1317, D-85741 Garching, Germany

(Received 22 February 2005; accepted 31 March 2005; published online 16 June 2005)

The paper presents a theoretical study of the low-energy dynamics of radiative association processes in the $He^+ + H_2$ collision system. Formation of the triatomic HeH_2^+ ion in its bound rotation-vibration states on the potential-energy surfaces of the ground and of the first excited electronic states is investigated. Close-coupling calculations are performed to determine detailed state-to-state characteristics (bound ← free transition rates, radiative and dissociative widths of resonances) as well as temperature-average characteristics (rate constants, photon emission spectra) of the two-state $(X \leftarrow A)$ reaction $He^+(^2S) + H_2(X^1\Sigma_g^+) \rightarrow HeH_2^+(X^2A') + h\nu$ and of the single-state $(A \leftarrow A)$ reaction $He^+(^2S) + H_2(X^1\Sigma_g^+) \rightarrow HeH_2^+(A^2A') + h\nu$. The potential-energy surfaces of the X- and A-electronic states of HeH_2^+ and the dipole moment surfaces determined *ab initio* in an earlier work [Kraemer, Špirko, and Bludsky, Chem. Phys. **276**, 225 (2002)] are used in the calculations. The rate constants $k(T)$ as functions of temperature are calculated for the temperature interval $1 \leqslant T \leqslant 100$ K. The maximum $k(T)$ values are predicted as $3.3 \times 10^{-15}\ s^{-1}\ cm^3$ for the $X \leftarrow A$ reaction and $2.3 \times 10^{-20}\ s^{-1}\ cm^3$ for the $A \leftarrow A$ reaction at temperatures around 2 K. Rotationally predissociating states of the $He^+ - H_2$ complex, correlating with the $v = 0$, $j = 2$ state of free H_2, are found to play a crucial role in the dynamics of the association reactions at low temperatures; their contribution to the $k(T)$ function of the $X \leftarrow A$ reaction at $T < 30$ K is estimated as larger than 80%. The calculated partial rate constants and emission spectra show that in the $X \leftarrow A$ reaction the $HeH_2^+(X)$ ion is formed in its highly excited vibrational states. This is in contrast with the vibrational state population of the ion when formed via the $(X \leftarrow X)$ reaction $He(^1S) + H_2^+(X^2\Sigma_g^+) \rightarrow HeH_2^+(X^2A') + h\nu$. © *2005 American Institute of Physics*. [DOI: 10.1063/1.1924453]

I. INTRODUCTION

It has been pointed out previously[1,2] that the HeH_2^+ ion, apart from its potential astrophysical relevance, is one of the simplest examples for which high-level theoretical calculations can be performed and directly compared with experimentally derived spectroscopic properties, as far as they are available, and with experimental measurements of its reactive behavior.

Recently, as the first attempt to rigorously calculate the dynamics of the radiative association (RA) reaction for a triatomic system, the reaction

$$He(^1S) + H_2^+(X^2\Sigma_g^+) \rightarrow HeH_2^+(X^2A') + h\nu \tag{1}$$

was investigated on a highly accurate level of theory and the results were reported in Ref. 1, hereafter called paper I. Now we initiate investigations on the same accuracy level of the dynamics of the radiative processes originating from the collision system $He^+ + H_2$, in other words, of the radiative processes starting from the excited electronic state potential of HeH_2^+. First, in the present paper, the two radiative association reactions stabilizing the $He^+ + H_2$ system are investigated, especially the reaction

$$He^+(^2S) + H_2(X^1\Sigma_g^+) \rightarrow HeH_2^+(X^2A') + h\nu, \tag{2}$$

as well as

$$He^+(^2S) + H_2(X^1\Sigma_g^+) \rightarrow HeH_2^+(A^2A') + h\nu, \tag{3}$$

where this latter reaction for the excited state is formally an analog to (1), i.e., the reaction product in this case is the complex $He^+ - H_2$ in vibration-rotation states lying below the $He^+ + H_2$ dissociation level of the excited state. Reaction (2), however, is the main focus of the present study. This type of reaction has previously been characterized as a two-state process and according to experience from earlier calculations for the simple diatomic HeH^+ ion[3,4] its reaction rate constant can be expected to be much larger than those of single-state reactions (1) and (3).

Whereas the above-mentioned reactions are generally believed to be of minor astrophysical importance, it is the other radiative process originating from the $He^+ + H_2$ collision system, the radiative charge transfer (RCT) reaction

$$He^+(^2S) + H_2(X^1\Sigma_g^+; v = 0) \rightarrow He(^1S) + H_2^+(X^2\Sigma_g^+; v'), \tag{4}$$

which could possibly play a role in astrophysical environments because it can provide an efficient cooling mechanism in the primordial gas chemistry. This reaction will be the subject of a forthcoming paper. For its rigorous state-to-state

---

[a] Electronic mail: felicja@phys.uni.torun.pl

quantum-mechanical treatment a detailed quantitative insight into reactions (2) and (3) is necessary.

Reaction (4) has been studied experimentally by Schauer *et al.* using an ion trap technique.[5] In order to rationalize the experimental results for its reaction rate at temperatures below 40 K, the following assumptions about its reaction mechanism have previously been made.[5–7]

(i) The process is practically entirely driven by radiative coupling between the lowest excited and the ground electronic states, whereas nonadiabatic coupling is unimportant.

(ii) Complex formation in the excited state, or rather the formation of rotationally predissociating states does not have much impact on the rate of the reaction.

(iii) The rate of the accompanying RA reaction, Eq. (2), which is involves the same collision partners as (4) is negligibly small.

The radiative mechanism of charge transfer in $He^+ + H_2$ thermal collisions postulated in the first assumption was originally proposed by Hopper[7] who, investigating the ground and the lowest excited electronic states of the HeH_2^+ ion, found a shallow $He^+ - H_2$ ion-molecule polarization well on the potential-energy surface of the first excited electronic state with a T-shaped geometry. Assumptions (ii) and (iii) were implicitly made by Kimura and Lane in their early theoretical study[6] of RCT reaction (4). Namely, in the simple reaction model which was adopted in this study no energy flow to diatomic rotation was possible, neither in the reactant nor in the product channel, and radiative transitions from the vibrational continuum of the excited state to all continuum and bound vibrational states of the ground electronic state were accounted for by means of the optical potential. The calculated rate constants, describing the RCT and RA reactions together, appeared reasonably consistent with the values measured for RCT. This fact was quoted in the discussion of Ref. 5 as supporting the hypothesis that the role of the complex formation in the RCT reaction is negligible.

Concerning assumption (i), it is now a well-established fact that the two lowest electronic states of the HeH_2^+ ion are well separated from each other over the entire range of their potentials important in low-energy collisions. Only for processes at higher collision energies has it been shown that nonadiabatic couplings between the lowest electronic states of A' symmetry become important.[8] However, assumptions (ii) and (iii) raise some doubts as to their validity, the latter because RA reaction (2) is a two-state process with usually non-negligible rate constant values, and the former because there is some evidence that rotational excitation of H_2 in collisions with He^+ can play an important role in the low collision energy regime. The evidence comes mostly from the investigations of the HeH_2^+ ion in its ground electronic state which have shown that rotation of the H_2^+ subunit is a crucial factor in the dynamics of the system. Numerous calculations of its vibration-rotation energy spectrum have revealed a considerable mixing of j states of H_2^+ within the ion.[1,2,9–12] Rotations (and vibrations) of the H_2^+ ions in collisions with He atoms were treated rigorously in our recent study of RA reaction (1). It was found that the number of quasibound states that contribute appreciably to the rate constant of this triatomic reaction is considerably increased as compared to the number of resonances driving the RA processes in the diatomic $He + H^+$ and $He^+ + H$ collision systems.[13–15] In addition, recent calculations[2] of $J = 0 - 2$ quasibound rotation-vibration energy levels of the excited electronic state of HeH_2^+ indicate that the number of resonances and their role in reactions (2) and (3) may be even larger.

The leading mechanism for the formation of the excited-state resonances, already predicted in the first qualitative characterization of the polarization well,[7] is a temporary conversion of kinetic energy of the relative motion in the $He^+ + H_2(v=0, j=0)$ collision system into rotation of H_2, i.e., the rotational predissociation mechanism. It is quite likely that these resonances substantially enhance the rate of the RA reactions at low temperatures. The effect may be comparable to or even larger than the enhancement caused by shape resonances. If this proves to be true, the implication will be that the contribution of rotationally predissociating states to the RCT reaction, which was neglected in the model of Ref. 6, could be rather large.

The present state-to-state calculations for RA reactions (2) and (3) provide a sufficiently accurate and reliable quantitative basis which allows us to discuss the points mentioned above. Emphasis is put on investigating the role of rotational predissociation especially on RA reaction (2). The accompanying study of reaction (3) is intended to assist in exhibiting the most characteristic features of the nuclear dynamics in the excited and ground electronic states and in resolving the impact of these features on the rates of radiative transitions between the states. Information of this kind may be valuable in the forthcoming attempt to devise a more realistic model for radiative charge transfer reaction (4). Altogether, the present study is hoped to contribute to an extension of the existing theoretical description of the HeH_2^+ system.

The electronic structure input needed for studying reactions (1)–(4), the potential-energy surfaces of the ground and the first excited electronic states of HeH_2^+, the corresponding dipole moment surfaces, and the transition dipole moment surface, have been calculated previously *ab initio* and are available in terms of analytic fits.[2,16]

Throughout the paper, the ground and the first excited electronic states of HeH_2^+ are called the X- and the A state, respectively. The three RA reactions: (1), (2), and (3), are referred to as $X \leftarrow X$, $X \leftarrow A$, and $A \leftarrow A$ processes, respectively. The symbol $HeH_2^+(A)$ is used to denote the $He^+ - H_2$ complex in its "bound" and quasibound states [strictly, the states below $He^+ + H_2(v=0, j=0)$ threshold are electronic resonances]. The symbol $HeH_2^+(X)$ denotes the ion in its (truly) bound and (purely) rovibrational quasibound states. Occasionally, the $HeH_2^+(X)$ ion is viewed as an $He - H_2^+$ complex.

Content of the paper

A detailed overview of the quantum theory of radiative association in application to atom-diatom systems was given in paper I. Apart from treating the association as an effect of weak interaction with the radiation field, three major assumptions are made in the theory to describe the initial and final molecular states in the process, all three being well justified in the energy range of interest here: (1) the nuclear motion is determined by a single potential-energy surface (PES), (2) the initial, scattering states lie sufficiently close to the lowest atom-diatom dissociation limit of the respective PES of the triatomic system so that they cannot be affected by the presence of other fragmentation limits of this PES, and (3) spin rotation and hyperfine interactions can be ignored. The formulas derived for the rate constant, emission spectrum, and radiative widths of long-living rotation-vibration resonances are briefly summarized here in Sec. II in terms of their application to the $He^+ + H_2$ system. Section III provides the necessary information on the computational methodology exploited in realization of the particular tasks of the present study. The main task, i.e., evaluation of the rate constants of reactions (2) and (3), is fully accomplished by the approach elaborated in paper I. The approach is based on the standard formulation of close-coupling equations for an atom–diatom system in a body-fixed reference frame using a *diabatic* basis set (CC-BF-diabatic). Its effective implementation relies on the exploitation of algorithms of the generalized log-derivative method.[17] Since the complete description of this CC-BF-diabatic approach can be found in Refs. 1 and 18, only some notations and necessary details on the accuracy controlling parameters used in the present calculations are given here in Sec. III A. An additional task arises from the need to get an insight into the dynamics of processes (1)–(3) which would permit an analysis of the calculated characteristics. To this end a possibly meaningful labeling of terminal states of transitions involved in the processes is needed, strictly, of bound and long-living quasibound states of the $HeH_2^+(X)$ and the $HeH_2^+(A)$ ions. It is of crucial importance in the assignment of appropriate quantum numbers, particularly to states of $HeH_2^+(X)$, to have an adequate measure for the separability of the He–H_2 bending motion from He–H_2 (and H–H) stretching motion(s). A procedure is developed for this purpose in which use is made of properties of natural expansions of multimode vibrational functions.[19–21] A description of the assignment procedure is given in Sec. III B. In Sec. IV, the most important results of the present close-coupling calculations of the $X \leftarrow A$ and $A \leftarrow A$ RA processes are summarized and discussed. Apart from the rate constants of the processes in the temperature range of 1-100 K and exemplary photon emission spectra (also from the $X \leftarrow X$ process), the results presented include the energies of all bound states of the He^+–H_2 complex as well as the energies and widths, nonradiative and radiative, of quasibound states in the range up to 300 cm^{-1} above the $He^+ + H_2(v=0, j=0)$ threshold. In Secs. IV A and IV B, a characterization of the rotation-vibration energy spectrum of the $He^+ - H_2$ complex and its comparison with the spectrum of the charge-transferred complex $He - H_2^+$ are provided. A detailed analysis of tendencies (propensity rules) among bound $\leftarrow$ resonance transition rates (radiative widths of resonances) in the two-state and in the two single-state RA processes, (1) and (3), is presented in Sec. IV C. A comparison of the temperature-averaged characteristics of the three processes, in particular, of the photon emission spectra, is given in Sec. IV D. Finally, in Sec. V, the overall reliability of the present results is assessed, answers to the questions posed above are given, cf. assumptions (ii) and (iii), and their significance is briefly discussed.

II. AN OUTLINE OF THEORY

A. Radiative association rate constant

We consider a gas mixture of He^+ ions and H_2 molecules at thermal equilibrium with temperature T and concentrate on the formation of HeH_2^+ ions due to spontaneous photon emission according to the reaction described in Eq. (2). The increase of the number density of HeH_2^+ ions with time is proportional to the product of the number densities of the reactants,

$$\frac{d}{dt} n_{HeH_2^+} = k n_{H_2} n_{He^+}, \tag{5}$$

and the proportionality constant k is the association rate constant, where k is the sum of the rates k^I for $I=0$ and $I=1$ which describe the association of He^+ with para- and orthohydrogen, respectively. Each k^I can be resolved further into partial rates,

$$k^I = \sum_{\mathcal{B}} k^I_{\mathcal{B}} = \sum_{\mathcal{B}} \sum_{vj} k^I_{\mathcal{B} \leftarrow vj}, \tag{6}$$

where $k^I_{\mathcal{B}}$ gives the efficiency of the formation of the $HeH_2^+(I)$ ions in state(s) with definite energy E^B, and $k^I_{\mathcal{B} \leftarrow vj}$ describes the situation when also the vibration-rotation energy of H_2 reactants is specified as ε_{vj} with v and j for the respective vibrational and rotational quantum numbers; j assumes even (odd) values for $I=0(1)$. The rate constant $k^I_{\mathcal{B} \leftarrow vj}$ is obtained as a function of T by averaging the bound $\leftarrow$ free transition rate $\frac{\partial}{\partial E} R^I(E^B; E, vj)$ over a canonical ensemble. The rate $\frac{\partial}{\partial E} R^I(E^B; E, vj)$, related by a simple kinematic factor to the cross section[22] $\sigma^I_{\mathcal{B} \leftarrow vj}(E)$, cf. paper I, describes the association under the conditions that the energy of relative translational motion of He^+ and H_2 is specified in addition to the internal energy ε_{vj} so that the total energy of the reactants (in the center-of-mass system) is in the range $[E, E+dE]$. Thus we have

$$k^I_{\mathcal{B} \leftarrow vj}(T) = \int P^I(E,T) \frac{\partial R^I(E^B; E, vj)}{\partial E} dE, \tag{7}$$

where $P^I(E,T)$ denotes the population of the states with energy E (per unit volume of the gas and for unit densities of the reactants),

$$P^I(E,T) = \frac{g^I}{Z(T)} \left(\frac{2\pi\hbar^2}{\mu k_B T} \right)^{3/2} \exp(-E/k_B T), \tag{8}$$

here $Z(T) = \sum_{vj} g_j (2j+1) \exp(-\varepsilon_{vj}/k_B T)$ with $g_j = g^0 = \frac{1}{4}$ for even j and $g_j = g^1 = \frac{3}{4}$ for odd j, μ is the reduced mass of the $He^+ + H_2$ system, and k_B is the Boltzmann constant.

Since the total angular momentum is preserved in the bound states of the HeH_2^+ ion and these states possess definite parity, the bound $\leftarrow$ free transition rate $\frac{\partial}{\partial E} R^I(E^B; E, vj)$ is resolved into contributions of transitions from the continuum states of the $He^+ + H_2$ system which are also characterized by a definite total angular momentum and (spectroscopic) parity quantum numbers, J and p, respectively. There are three $J^Bp^B \leftarrow Jp$ transitions possible to a given bound state of the ion, i.e.,

$$\frac{\partial R^I(E^B;E,\upsilon j)}{\partial E}=\sum_{J=J^B-1}^{J^B+1}(2J+1)\frac{\partial R^I(E^BJ^Bp^B;EJp,\upsilon j)}{\partial E}, \qquad (9)$$

with $p=p^B(-1)^{J+J^B+1}$. The rates of the individual transitions are expressed in terms of partial bound←free transition amplitudes $T^I_{\upsilon jl}(E^BJ^Bp^B;EJp)$,

$$\frac{\partial R^I(E^BJ^Bp^B;EJp,\upsilon j)}{\partial E} = \frac{4}{3\hbar^4c^3}(E-E^B)^3\sum_l |T^I_{\upsilon jl}(E^BJ^Bp^B;EJp)|^2, \qquad (10)$$

which are reduced matrix elements of the appropriate transition dipole moment vector $\{d_q;q=-1,0,1\}$,

$$T^I_{\upsilon jl}(E^BJ^Bp^B;EJp)\overset{\rm def}{=}\sqrt{\frac{2J^B+1}{2J+1}} \times\frac{\langle E^BJ^BM^Bp^B|d_q|E^+JMp,\upsilon jl\rangle}{C(J1J^B,MqM^B)}, \qquad (11)$$

$|E^+JMp,\upsilon jl\rangle$ denote (energy normalized) partial scattering states of the He^++H_2 system with M being the quantum number of the projection of the total angular momentum on the space-fixed (SF) Z axis; the numbers behind the comma (υjl) characterize the state before scattering, l specifies the angular momentum of the relative motion, and $C(\ldots,\ldots)$ denotes the Clebsch–Gordan coefficient. c in Eq. (10) denotes the speed of light.

B. Emission spectrum

The power emitted at temperature T by the considered gas, contained in a volume V, due to RA reaction (2) is given by $\mathcal{I}(T)n_{H_2}n_{He^+}V$. The factor $\mathcal{I}(T)$ is the emission intensity which can be written as the integral $\mathcal{I}(T)=\int\mathcal{I}(\nu,T)d(h\nu)$ with $\mathcal{I}(\nu,T)$ denoting the spectral density of emission, a quantity of dimension of power/energy × volume, cf. Ref. 23. $\mathcal{I}(\nu,T)$ can be resolved into terms which describe the emission arising from the formation of $HeH_2^+(I=0)$ and $HeH_2^+(I=1)$ in different states $\mathcal{B}$, i.e., $\mathcal{I}=\Sigma_I\Sigma_{\mathcal{B}}\mathcal{I}^I_{\mathcal{B}}$. The term $\mathcal{I}^I_{\mathcal{B}}(\nu,T)$ is simply related to the bound←free transition rates, viz.,

$$\mathcal{I}^I_{\mathcal{B}}(\nu,T)d(h\nu)=h\nu P^I(E,T)\sum_{\upsilon j}\frac{\partial R^I(E^{\mathcal{B}};E,\upsilon j)}{\partial E}dE, \qquad (12)$$

with $h\nu=E-E^B$.

C. Resonance contribution

Quasibound vibration-rotation states of the He^+-H_2 complex manifest themselves as sharp structures of the rates $\frac{\partial}{\partial E}R^I(E^BJ^Bp^B;EJp,\upsilon j)$ as functions of the energy E. Very sharp peaks are approximated by δ functions,

$$\frac{\partial R(\mathcal{B};EJp,\upsilon j)}{\partial E}\approx\frac{1}{\hbar}\Gamma^{\rm rad}_{\mathcal{B}}\delta(E-E^{\rm res})\frac{\Gamma_{\upsilon j}}{\Gamma^{\rm tot}}, \qquad (13)$$

where $E^{\rm res}$ is the resonance energy, $\Gamma_{\upsilon j}$ and $\Gamma^{\rm rad}_{\mathcal{B}}$ are the resonance partial widths, nonradiative and radiative, respectively, and $\Gamma^{\rm tot}=\Gamma+\Gamma^{\rm rad}$ with $\Gamma=\Sigma_{\upsilon j}\Gamma_{\upsilon j}$ and $\Gamma^{\rm rad}=\Sigma_{\mathcal{B}}\Gamma^{\rm rad}_{\mathcal{B}}$. The index I is omitted and the abbreviation $\mathcal{B}\overset{\rm def}{=}(E^BJ^Bp^B)$ is used hereafter. The partial radiative width $\Gamma^{\rm rad}_{\mathcal{B}}$ is given by the formula

$$\Gamma^{\rm rad}_{\mathcal{B}}=\frac{4}{3\hbar^3c^3}(E^{\rm res}-E^{\mathcal{B}})^3|T(\mathcal{B};\mathcal{R})|^2, \qquad (14)$$

where $T(\mathcal{B};\mathcal{R})$ represents a bound←resonance transition amplitude. It is defined analogously to $T^I_{\upsilon jl}(E^BJ^Bp^B;EJp)$, i.e., by Eq. (11) in which the partial scattering state at $E=E^{\rm res}$ is replaced by an appropriate bound state of energy close to $E^{\rm res}$, cf. paper I. The approximation of Eq. (13) leads to (an approximate) resolution of the rate constant k into resonance and background terms, $k(T)\approx k^{\rm res}(T)+k^{\rm back}(T)$ with $k^{\rm res}(T)=\Sigma_{\mathcal{B}}\Sigma_{\mathcal{R}}k_{\mathcal{B}\leftarrow\mathcal{R}}(T)$, and to the following formula[24] for the contribution of individual $\mathcal{B}\leftarrow\mathcal{R}$ transition:

$$k_{\mathcal{B}\leftarrow\mathcal{R}}(T)=\frac{1}{\hbar}P(E^{\rm res},T)(2J+1)\Gamma^{\rm rad}_{\mathcal{B}}\frac{\Gamma}{\Gamma^{\rm tot}}. \qquad (15)$$

The resonance contribution to the emission spectrum density can be presented in terms of the following averages in subsequent intervals $[\nu_i,\nu_i+\Delta\nu]$ of photon frequency:

$$\overline{\mathcal{I}}^{\rm res}(\nu_i,\Delta\nu;T)=\frac{1}{\Delta\nu}\sum_{\mathcal{B}}\sum_{\mathcal{R}}\nu_{\mathcal{BR}}k_{\mathcal{B}\leftarrow\mathcal{R}}(T)\,\theta(\nu_i+\Delta\nu-\nu_{\mathcal{BR}})\,\theta(\nu_{\mathcal{BR}}-\nu_i), \qquad (16)$$

where $\nu_{\mathcal{BR}}=(E^{\rm res}-E^{B})/h$ and θ is the Heaviside function.

III. COMPUTATIONAL ASPECTS

A. Some details on the CC-BF-diabatic approach

The configuration of the nuclear centers in the He^++H_2 system is described in terms of the Jacobi vectors $\boldsymbol{r}$, joining the H nuclei, and $\boldsymbol{R}$, pointing from the center of mass of H_2 towards the He nucleus, whereas the angle between these vectors is denoted by θ. The motion is described relative to the BF reference frame with the Z axis directed along the vector $\boldsymbol{R}$. The coupled radial equations (in $R=|\boldsymbol{R}|$ coordinate) for the rovibrational bound and free states of the He^++H_2 system are constructed using parity-adapted total angular momentum eigenfunctions [cf. Eqs. (17) and (18) below] and radial functions (in $r=|\boldsymbol{r}|$ coordinate) of the rovibrational states of free H_2. The equations in a set for a given pair J and p are enumerated by three quantum numbers: υ, j, and λ, the latter being the absolute value of the projection of the angular momentum on the Z axis. The size N of the coupled equation sets is reduced by imposing a limit $\lambda_{\rm max}$ on the λ number which introduces an extra approximation (Coriolis-coupling reduction) into the close-coupling approach to states with $J>\lambda_{\rm max}$. However, as has been demonstrated in paper I, a sufficiently accurate description of the dynamics of the $He+H_2^+$ system on the lowest part of the X-state potential surface was achieved there with $\lambda_{\rm max}=4$. There is a good reason to expect that the same range of λ values can assure even a better accuracy in describing the $He^+ + H_2$ system in the well region of the A-state potential because the anisotropy of the interaction potential is smaller in this case.

The coupled equations for $He^+ + H_2(I)$ were formulated in the bases involving 28 rovibrational states of H_2: with $v = 0$, 1, 2, 3 and $j = 0$, 2, …, 12 for $I = 0$ and $j = 1$, 3, …, 13 for $I = 1$. The radial functions of the states were generated from an appropriate asymptotic part of the A-state PES. The maximal λ value allowed was $\lambda_{\max} = 3$ in (most of) the calculations on even j states and $\lambda_{\max} = 4$ in the calculations on odd j states. Thus, the maximal dimension of the coupled equations was $N = 124$. The coupled equations were usually integrated within the range of 1–17 Å. The energy range covered in the calculations extended from 817 cm^{-1} below up to 300 cm^{-1} above the lowest, $He^+ + H_2(v = 0, j = 0)$, dissociation limit.

B. Assignment of HeH_2^+ states: Applying natural expansion analysis (NEA)

Within the CC-BF-diabatic approach, the bound-state functions of HeH_2^+ are determined using the following expansions:

$$\Psi(E^B JMp; \boldsymbol{r}, \boldsymbol{R}) = \sum_{\lambda=\lambda_{\min}}^{\lambda_{\max}} \Psi_\lambda(E^B Jp; r, R, \theta)\Theta_\lambda^{JMp}(\alpha, \beta, \zeta), \tag{17}$$

$$\Psi_\lambda(E^B Jp; r, R, \theta) = \frac{1}{rR}\sum_{v}\sum_{j(\leqslant\lambda)} F_{vj\lambda}(E^B Jp; R)\chi_{vj}(r)\tau_{j\lambda}(\theta). \tag{18}$$

The first expansion describes rotation of the SF reference frame with respect to the body-fixed one whose Z axis is aligned to the vector $\boldsymbol{R}$, and Y axis is perpendicular to the plane of the three nuclei. α, β, and ζ are Euler angles of the rotation and $\Theta_\lambda^{JMp}(\alpha, \beta, \zeta)$ is related to Wigner's rotation matrix D^J,

$$\Theta_\lambda^{JMp}(\alpha, \beta, \zeta) \overset{\text{def}}{=} \left[\frac{2J+1}{16\pi^2(1+\delta_{\lambda 0})}\right]^{1/2} [D_{M\lambda}^{J*}(\alpha, \beta, \zeta) + p(-1)^\lambda D_{M-\lambda}^{J*}(\alpha, \beta, \zeta)].$$

The resulting probability distribution among allowed λ values [$\lambda_{\min} = 0(1)$ for $p = 1(-1)$ and $\lambda_{\max} \leqslant J$],

$$\rho_\lambda(E^B Jp) \overset{\text{def}}{=} \int_0^\infty R^2 dR \int_0^\infty r^2 dr \int_0^\pi \sin\theta\, d\theta \times |\Psi_\lambda(E^B Jp; r, R, \theta)|^2, \quad \sum_\lambda \rho_\lambda = 1,$$

provides information about the strength of Coriolis coupling in a given state $(E^B Jp)$. Existence of a maximum in ρ_λ that exceeds 0.5 is a good criterion for using the maximum position, denoted by k, as a label of the state. The second expansion, Eq. (18), gives a diabatic representation of the λ components of the function of the state $(E^B Jp)$ in terms of the matrix elements of the reduced rotation matrix d^j, i.e., $\tau_{j\lambda}(\theta) \overset{\text{def}}{=} \sqrt{(2j+1)/2}\, d_{\lambda,0}^j(\theta)$, and in terms of the vibrational functions $\chi_{vj}(r)$ of free diatom (H_2 or H_2^+). Thus, information on mixing of v- and j-diatomic states in the state $(E^B Jp)$ of the HeH_2^+ ion is obtained by inspecting the probability distributions $\rho_v(E^B Jp) \overset{\text{def}}{=} \Sigma_j \Sigma_\lambda \int |F_{vj\lambda}(E^B Jp; R)|^2 dR$ and $\rho_j(E^B Jp)$, defined analogously. For all bound states of both $HeH_2^+(X)$ and $HeH_2^+(A)$, the distributions ρ_v reveal maximal population of the $v = 0$ state, exceeding 90% in most cases. This indicates good separability of the r motion from the θ- and R motions and justifies labeling the states of both ions with the quantum number $v_r = 0$. For states of $HeH_2^+(A)$, the distributions ρ_j show also a dominance of one j state of H_2. Thus, the dominant j value, denoted by b, can be used to characterize the θ motion in a given state $(E^B Jp)$ of the $HeH_2^+(A)$ ion and then an appropriate quantum number v_R to label the R-stretching motion in this state is obtained by counting nodes in the radial function $F_{v_r bk}(E^B Jp; R)$.

Obviously, the diabatic representation used in the calculations and suitable for assigning the states of $HeH_2^+(A)$ cannot display equally clearly the character of atom-diatom motion in states of $HeH_2^+(X)$. This is because of the anisotropy properties of the X-state PES differing substantially from the properties of the A-state PES. As depicted in Fig. 1, the bending motion in the X state is governed by the potential barrier at the perpendicular configuration of the He nucleus relative to the H–H axis which is ca. 2.3 times higher than the barrier at the collinear configurations of the three nuclei in the A state. One thus expects a difference in character of this motion between states in the energy ranges below and well above the barrier top. There is certainly a substantial j mixing in the low-energy range. A sizable coupling with the stretching (R) motion can be expected in the intermediate range, close to the barrier top. Considering a change of the diabatic representation given by Eq. (18), it is expedient to use natural expansions which are known[19–21] to provide the most rigorous characterization of separability of (square integrable) functions in given coordinates. Thus, the functions $\Psi_\lambda(E^B Jp; r, R, \theta)$ are reexpanded in terms of natural orbitals in all three coordinates:

$$\Psi_\lambda(r, R, \theta) = \sum_i \sqrt{a_i^\lambda}\, h_i^\lambda(r)\, \psi_i^\lambda(R, \theta) \quad \text{and}$$

$$\psi_i^\lambda(R, \theta) = \sum_m \sqrt{c_{im}^\lambda}\, f_{im}^\lambda(R)\, t_{im}^\lambda(\theta);$$

the orbitals $h_i^\lambda(r)$ for $i = 1$, 2, … are eigenfunctions of the density kernel $\rho_\lambda(r, r')$,

$$\rho_\lambda(r, r') \overset{\text{def}}{=} rr' \int R^2 dR \int_0^\pi \sin\theta\, d\theta\, \Psi_\lambda(r, R, \theta)\Psi_\lambda(r', R, \theta) = \sum_i h_i^\lambda(r) a_i^\lambda h_i^\lambda(r'),$$

to the eigenvalues a_i^λ which satisfy the relation $\Sigma_i a_i^\lambda = \rho_\lambda$. The orbitals $f_{im}^\lambda(R)$ and $t_{im}^\lambda(\theta)$ for $m = 1$, 2, … come from diagonalization of the respective kernels $\rho_i^\lambda(R, R')$ and $\rho_i^\lambda(\theta, \theta')$, calculated using the function $\psi_i^\lambda(R, \theta)$. The common eigen-

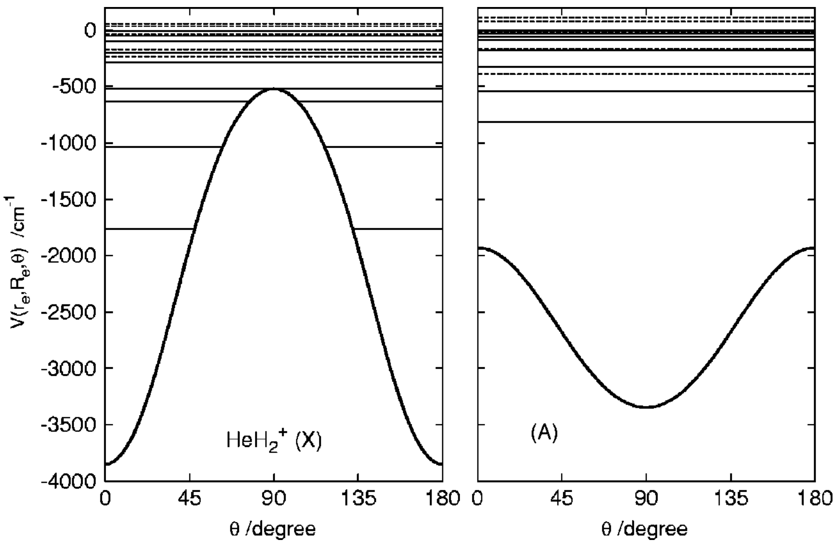

FIG. 1. Left: Cut of X-state potential at optimum bond distances $r_e = 1.0981$ Å and $R_e = 1.573$ Å. Zero of energy corresponds to the $He + H_2^+(v=0, j=0)$ dissociation threshold. Energy levels of the $J=0$ bound state of $HeH_2^+(I)$ for $I=0$ and $I=1$ are shown with solid and dashed lines, respectively. For the four lowest levels, the splitting between $I=0$ and $I=1$ values is too small to be visible in the figure (see Table II and Fig. 2). Right: Same for A-state potential $r_e = 0.7480$ Å and $R_e = 2.387$ Å. $E=0$ corresponds to the $He^+ + H_2(v=0, j=0)$ threshold.

values c_{im}^{λ} of the two latter kernels satisfy $\Sigma_m c_{im}^{\lambda} = 1$ for each i. The number $a_i^{\lambda} c_{im}^{\lambda}$ times 100% gives the occupancy of the natural configuration $h_i^{\lambda}(r) f_{im}^{\lambda}(R) t_{im}^{\lambda}(\theta)$ in the total function of the investigated state. The aforementioned good separability of the r motion from θ- and R motions manifests itself by the fact that the largest eigenvalue a_i^{λ}, numbered with $i=1$, is close to ρ_{λ}. Thus, only the configurations with $i=1$, ordered so that $b_{11} \geqslant b_{12} \geqslant b_{13} \geqslant \ldots$ are chosen for further examination. The numbers of nodes (n_r, n_R, and n_{θ}) in the orbitals forming the most occupied configurations (with $m=1$, 2) are converted to vibrational quantum numbers v_r, v_R, and v_{θ} or b. Obviously, $v_r = n_r$ and $v_R = n_R$. Two numbers are needed to distinguish the θ orbitals. Namely, for orbitals strongly localized around collinear configurations, being combinations of several functions $\tau_{j\lambda}(\theta)$ (with j even or odd for $I=0$ and 1, respectively), it is appropriate to define $v_{\theta} = n_{\theta}$ and $v_{\theta} = n_{\theta} - 1$ for $\lambda + I$ even and odd, respectively. Then $v_{\theta} + \lambda$ correlates with the vibrational number of circular harmonic oscillator and λ corresponds to the vibrational angular momentum. However, if a given orbital reveals small j mixing, i.e., $t_{1m}^{\lambda}(\theta) \approx \tau_{b\lambda}(\theta)$, then it is most naturally assigned with the leading j value, i.e., with $b = n_{\theta} + \lambda$. There is, of course, a simple connection between the two numbers v_{θ} and b ($b = v_{\theta} + \lambda$ and $b = v_{\theta} + \lambda + 1$ for even and odd $\lambda + I$, respectively). However, by choosing one of the symbols one can indicate the type of θ motion in a given configuration; whether it is more like vibrations of a semirigid linear molecule or more like (adiabatically invariant) rotations of diatom within an atom–diatom complex of case 2, cf. Ref. 25.

IV. RESULTS AND DISCUSSION

A. Bound states of $HeH_2^+(X)$

All 536 bound states of HeH_2^+ supported by the PES of X state[2] were determined in paper I. The states were classified into 61 rovibrational groups, designated with the quantum numbers I, p, and k, and with a collective index $[v]$ for the three (r, θ, R) vibrational modes [Table I(A)]. A closer examination of the vibrational motion is undertaken in this work applying the natural expansion analysis of functions of $J=k$ states from the particular $(I, [v], k, p)$ groups, called hereafter "vibrational" states. The pattern of the corresponding energy levels with their v_{θ} and v_R quantum number assignments are displayed in Fig. 2. Details on the natural expansions of the investigated functions, such as occupancies of the two leading configurations and numbers of nodes in their θ- and R orbitals, are given in Table II. Some characterization of rotational structure of the few lowest $(I=0, [v], k, p)$ groups ($[v] = 1-3$) is provided in Table III.

As displayed in Fig. 1 for $J=0$ and in Fig. 2 for all $J = k = 0-3$ bound states of $HeH_2^+(X)$, there is a clear distinction between the energy level patterns in the ranges below and above the top of the barrier at $\theta = 90°$. The patterns for j even and j odd states are identical in the lower range but depart from each other above. The spacings between the lowest levels of the ground stretching state ($v_R = 0$), i.e., $(v_{\theta}, k) = (0,0)$, (0, 1), (0, 2), and (2, 0), are not much different from those between 0^0, 1^1, 2^2, and 2^0 levels of semirigid linear molecules (or case 3 atom–diatom complexes according to Ref. 25). Above the barrier in states with an excited stretching mode, the bending vibrations become more and more delocalized because the H_2^+ subunit of the ion tends to rotate more freely. In states with $v_R \geqslant 3$, close to the dissociation limits of the para- and orthoions, the rotation is essentially free. These states are marked in Table II.

The results in Table II confirm that in states above the barrier the separability between the bending and stretching modes is considerably reduced. The occupancies of the leading configurations in the functions of ($[v]=3$, $k=0$, 1) states, with $v_{\theta}=2$ or $v_R=2$, drop by about 20% below the occupancies of $(v_{\theta}, v_R) = (0,0)$, (0, 1) configurations in $[v]=1$, 2 states. This trend is amplified in higher excited states ($[v] = 4-7$) in which an increasing mixing of mostly two different bending-stretching configurations is observed. The mixing is facilitated by the fact that the fundamental bending and stretching frequencies do not differ much from each other, cf. Table III.

The general characterization of the higher excited states given here is actually consistent with what was already noted in the first calculations[9] on rotation-vibration states of $HeH_2^+(X)$. The present analysis adds to the previous qualitative description a quantitative measure for the size of the

TABLE I. (A) Bound states $\mathcal{B}=([\upsilon],k,J,p)$ of the $HeH_2^+(I)$ ion, $I=0$, 1, on the PESs of the X- and A-electronic states. Classification into rovibrational groups $(I,[\upsilon],k,p)$. (B) Count of $J\leftarrow J\pm1$, J bound←free transitions involved in the $X\leftarrow A$ and $A\leftarrow A$ processes.

(A)	$I=0$ (j even)						$I=1$ (j odd)						
	$p=1$			$p=-1$			$p=1$				$p=-1$		
X state	$k=0$	1	2	$k=1$	2	3	$k=0$	1	2	3	$k=1$	2	3
No. of states	103	41	16	67	37	4	106	62	16	2	64	16	2
Max$[\upsilon]$[a]	9	4	2	8	6	1	9	8	2	1	8	2	1
Max J[b]	20	16	11	17	13	6	21	16	11	4	16	11	4
A state	$k=0$	1	2	$k=1$	2	4	$k=0$	1	2	3	$k=1$	2	3
No. of states	103	14	29	63	99	5	52	100	6	14	100	6	14
Max$[\upsilon]$[a]	9	2	3	6	9	1	5	9	1	2	9	1	2
Max J[b]	20	11	16	18	22	8	16	21	7	13	21	7	13

(B)	Transitions $R,P,Q=J\leftarrow J-1,J+1,J$			
$X\leftarrow A$				
No. of R,P	311	*208*[c]	363	156
No. of Q	*151*[c]	108	177	82
$A\leftarrow A$				
No. of R,P	283	*328*[c]	339	231
No. of Q	*237*[c]	59+*102*[d]	167	120

[a] $[\upsilon]$ enumerates different $J=k$ states among the ones assigned with given k and p. The enumeration is according to energy of the states, starting from $[\upsilon]=1$ for the lowest energy.

[b] J value of the highest bound state in the $[\upsilon]=1$ group.

[c] Energy threshold of the initial states of these transitions lies at 354.03 cm^{-1}, cf. Table IV. The transitions contribute negligible amounts to the rate constants at temperatures below 100 K and therefore were not taken into account in the calculations.

[d] Italic number denotes transitions to bound states of energies above 100 cm^{-1}, omitted in the calculations.

mixing between the vibrational (θ- and R) modes and reveals that in several cases the mixing is substantial. Some care has therefore to be used when attempting to assign rovibrational states of the $HeH_2^+(X)$ ion. Simple extrapolations from the semirigid-molecule model to the excited states above the barrier may yield meaningless results.

Unlike the question about the separability of vibrational modes in bound states of $HeH_2^+(X)$, the Coriolis coupling between different λ components of the states has been discussed extensively in the previous studies on the ion (see paper I and references therein). Examples of effects generated by this coupling should be noted in Table II, such as the energy splitting between e- and f-symmetry states and the cases of the second most occupied natural configurations oc-

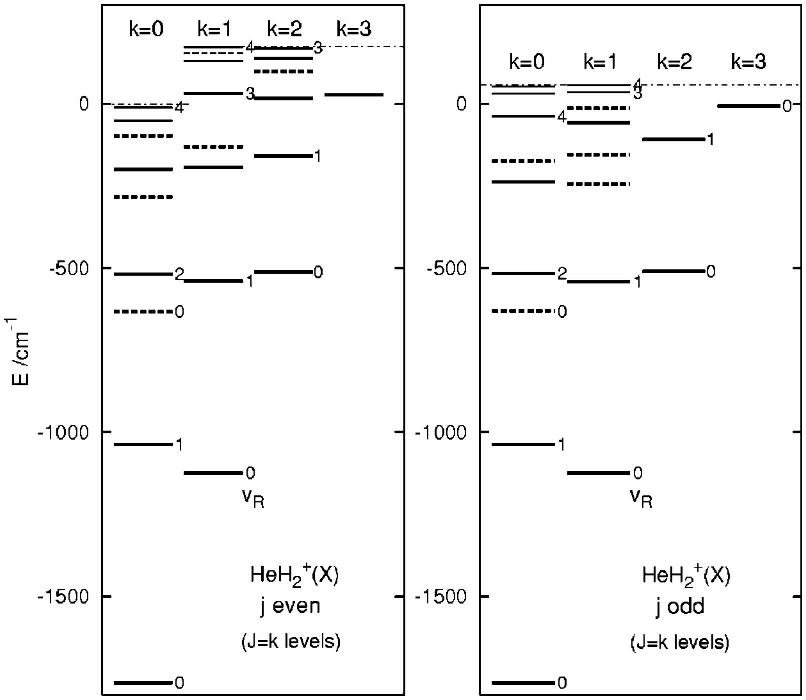

FIG. 2. Energy levels of bound “vibrational” states of $HeH_2^+(X)$. $He+H_2^+(\upsilon=0,j=0,1,2)$ thresholds are indicated by tiny dashed-dotted lines. All segments in $k\geqslant1$ columns represent two closely spaced (e,f) levels. (For even j, the e levels above $E=0$ pertain to quasibound states.) Segments drawn with a dashed line indicate states of predominantly $\upsilon_\theta=2$ character. Continuous segments denote $\upsilon_\theta=0$ states. The highest levels in the $k=0$, 1 columns, indicated by thinner lines, are labeled with $b=\upsilon_\theta+k+I$. The number υ_R is shown only in cases of good separability between R- and θ modes (when the occupancy of the leading natural configuration in the respective function exceeds 80%, see Table II).

TABLE II. Energies of bound “vibrational” states $(I,[v],k,J=k,p)$ of $\mathrm{HeH}_2^+(X)$. Analysis (NEA) of functions of the states: occupancies of two leading natural configurations in (r,θ,R)-coordinates and quantum numbers v_θ and v_θ assigned to them. $v_\theta=0$ in all cases. The energies are given in cm^{-1} relative to the $\mathrm{He}+\mathrm{HeH}_2^+(v=0,j=0)$ threshold. The dissociation limits of $p=-1$ states of $\mathrm{He}+\mathrm{HeH}_2^+(X;I=0)$ and of all $\mathrm{He}+\mathrm{HeH}_2^+(X;I=1)$ states lie at 174.20 cm^{-1} and 58.22 cm^{-1}, respectively. For $k\geqslant 1$, energies of $p=-1$ states are listed in E columns. Energies of $p=1$ states are shown relative to their $p=-1$ counterparts in $e-f$ columns. For $k>0$, NEA results of $p=-1$ states are shown.

		$I=0$						$I=1$					
k	$[v]$	E	$e-f$ [a]	$(v_\theta v_R)$ [b]	%	$(v_\theta v_R)$ [b]	%	E	$e-f$	$(v_\theta v_R)$ [b]	%	$(v_\theta v_R)$ [b]	%
0	1	−1763.5		(0 0)	100	[c]		−1763.5		(0 0)	100	[c]	
	2	−1037.2		(0 1)	99			−1037.2		(0 1)	99		
	3	−632.4		(2 0)	82	(0 2)	12	−630.3		(2 0)	82	(0 2)	12
	4	−518.1		(0 2)	86	(2 1)	14	−517.4		(0 2)	86	(2 1)	13
	5	−282.6		(2 1)	71	(0 3)	21	−236.5		(0 3)	60	(2 2)	36
	6	−199.2		(0 3)	74	(2 2)	18	−172.7		(2 2)	60	(2 1)	30
	7	−98.0		(2 1)	54	(0 4)	36	−38.5		(0^*4)	89		
	8	−51.1		(0^*3)	71	(4^*1)	17	31.6		(0^*5)	74	(2^*1)	14
	9	−11.0		(0^*4)	93			52.8		(0^*6)	65	(2^*2)	13
1	1	−1123.6	−0.3	(0 0)	99			−1123.7	−0.3	(0 0)	99		
	2	−538.7	−1.4	(0 1)	95			−541.3	−1.0	(0 1)	94		
	3	−192.7	−0.2	(0 2)	69	(2 1)	29	−244.0	−0.5	(2 0)	70	(2 2)	28
	4	−132.0	−0.0	(2 1)	75	(0 2)	20	−155.4	1.1	(2 1)	74	(0 2)	19
	5	32.4	*−1.1*	(0 3)	90			−56.5	−0.2	(0 3)	57	(2 2)	40
	6	131.5	*0.0*	(0^*4)	79	(2 2)	19	−12.8	0.4	(2 2)	56	(4 0)	28
	7	155.0	*−0.9*	(2^*3)	60	(2 3)	28	35.3	1.3	(0^*3)	92		
	8	173.0	*−0.5*	(0^*4)	96			57.6	0.4	(0^*4)	98		
2	1	−511.8	−0.0	(0 0)	80			−510.8	−0.8	(0 0)	85		
	[d]			(0 1)	17					(0 1)	13		
	2	−158.6	−0.0	(0 1)	83	(2 2)	12	−107.8	0.0	(0 1)	86		
	3	16.0	*−0.1*	(0 2)	73	(2 1)	24						
	4	99.7	*0.0*	(2 1)	68	(0 3)	27						
	5	140.7	*0.2*	(0 2)	71								
	[d]			(0 2)	13								
	6	170.2−	*0.2*	(0^*3)	91								
3	1	27.2	*−0.0*	(0 0)	56			−5.4	0.0	(0 0)	92		
	[d]			(0 2)	35								

[a] Italic numbers denote quasi-bound states.

[b] Asterisk marks cases of small j mixing for which the number b is better suited: $b=v_\theta+k$ and $b=v_\theta+k+1$ for even and odd $k+I$, respectively.

[c] The second configuration is shown only if its occupancy is larger than 10%.

[d] Configurations listed in the second lines occur in the $\lambda=k-1$ components of analyzed functions.

TABLE III. Energies of $J\geqslant k$ levels in selected $(I=0,[v],k,p)$ states of $\mathrm{HeH}_2^+(X)$. $p=-1$ in all $k>0$ cases. Parameters of fitting to the polynomial $E(J;k)=E^0+B(J;k)-D(J;k)^2+H(J;k)^3$ in $(J;k)\overset{\mathrm{def}}{=}J(J+1)-k^2$. Deperturbed values (see footnote [a]) are given (in the last two lines) for Coriolis coupled $(k,[v])=(1,2)$ and (2, 1) states. All parameters are in cm^{-1}.

k	$[v]$	$(v_\theta v_R)$	E^0	B	$D10^4$	$H10^6$	β [a]	dev [b]
0	1	(0 0)	0.00	4.08	3.74	−0.05		0.00
	2	(0 1)	726.29	3.68	2.78	0.72		0.01
	3	(2 0)	1131.12	3.88	14.66	−3.38		0.47
1	1	(0 0)	635.80	4.09	5.11	−0.14		0.00
1	2	(0 1)	1222.42	2.38	−59.21	−1415.70		139.0
2	1	(0 0)	1242.82	4.47	179.80	253.83		35.5
1	2	(0 1)	1231.75	3.44	7.80	−1.08	3.13	0.02
2	1	(0 0)	1229.02	3.94	9.09	−0.02	3.13	0.06

[a] Calculated $E(J)$ values for $J=2-6$ were fitted to eigenvalues of a 2×2 (symmetric) matrix having diagonal elements parametrized as $E(J;k=1)$ and $E(J;k=2)$, respectively, and off-diagonal elements in the form $\beta\sqrt{J(J+1)-2}$.

[b] Mean-square deviation between fitted and calculated values of $E(J;k)$ for $J=k,\ldots,k+10$.

TABLE IV. Energies of (“vibrational”) $J=k$ states of $HeH_2^+(A)$ below the $He^+ + H_2(v=0, j=0-2)$ thresholds. Assignment with quantum numbers b (correlating with j number of free H_2) and v_R. All energies are given relative to the $He^+ + H_2(v=0, j=0)$ threshold which lies 74507 cm^{-1} above $He + H_2^+(v=0, j=0)$ threshold of X state. $j=1$, $j=2$, and $j=3$ thresholds of A state lie at 118.37, 354.03, and 704.83 cm^{-1}, respectively. $p=-1$ parity states with b even are bound up to the $j=2$ threshold. b odd states of both parities are bound up to the $j=1$ threshold. For $k>0$, f levels are listed only. Among the bound $J=k$ states, the largest $e-f$ energy splitting, -0.3 cm^{-1}, occurs in the $(b,k,v_R)=(2,1,0)$ case.

	$I=0$					$I=1$			
	$b=0$	$b=2$			$b=4$	$b=1$		$b=3$	
v_R	$k=0$	$k=0$	$k=1$	$k=2$	$k=4$	$k=0$	$k=1$	$k=2$	$k=3$
0	−817.0	−55.5[a]	−264.0	−514.1	228.2	−390.5	−744.7	17.4	−214.5
1	−538.4		−22.3	−253.9		−168.1	−461.9		76.0
2	−326.3		152.0	−32.9		−13.6	−245.1		
3	−177.2		263.6	126.4		76.7	−90.3		
4	−83.2		323.9	232.0		114.9	10.5		
5	−31.9		348.4	295.3			69.3		
6	−9.1			329.2			99.4		
7	−1.1			345.9			113.2		
8				353.1			118.2		

[a] In the classification of Table I, this state belongs to the $(k=0,[v]=6)$ group. Consequently $(b=0,\ v_R=5, 6, 7)$ states belong to the $(k=0,\ [v]=7, 8, 9)$ groups.

curring in the $\lambda=k-1$ components of the analyzed functions. The example in Table III concerns perturbations in the progressions of rotational energy (J) levels of close f-symmetry states $(k,[v])=(1,2)$ and (2, 1). The perturbations are shown in terms of the anomalous values of the spectroscopic parameters which result when each progression is fitted separately to a polynomial in $J(J+1)-k^2$. A simple deperturbation procedure, described in the corresponding footnote, is applied to this case. Apart from correcting the parameters, it provides information on the strength of the Coriolis coupling between the two states (in terms of the parameter β).

B. Bound states of $HeH_2^+(A)$

Altogether 605 bound rovibrational states are found to be supported by the PES calculated for the excited electronic A state in Ref. 2; 313 states pertain to $HeH_2^+(A;I=0)$. An overall classification of the states is presented in Table I(A) together with that for the ground electronic state. The uniform labeling of the rovibrational groups of states in both electronic states (using the index $[v]$) is convenient in organizing the rate constant calculations. For a more complete characterization of $HeH_2^+(A)$, the quantum numbers v_r, b, and v_R composing $[v]$ are specified in Table IV. The pattern of energy levels of $J=k$ vibrational states is shown in Fig. 3. Table V lists the spectroscopic constants for some of the lower states (b,k,v_R) and provides an example for Coriolis coupling in the system.

The pattern of $J=k$ energy levels of $HeH_2^+(A)$ shown in Fig. 3 and in Table IV differs qualitatively from that of $HeH_2^+(X)$ particularly in two aspects. First, in the A state a

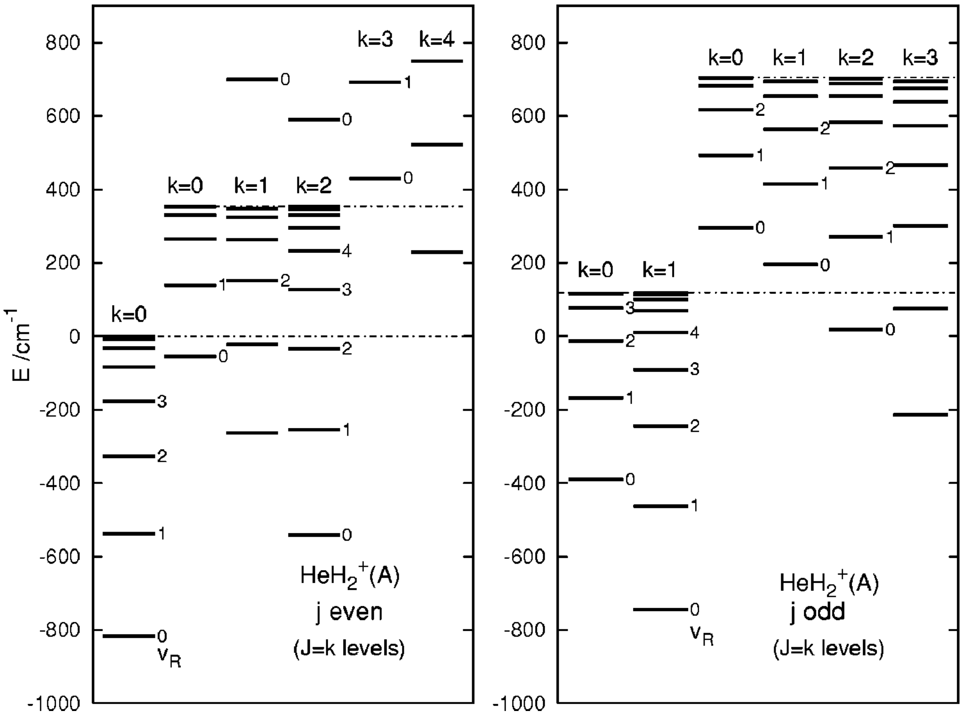

FIG. 3. Energies of $(v_r=0, b, v_R, k, J=k)$ states of $HeH_2^+(A)$ with $b=0-3$ lying below their respective $He^+ + H_2(v=0, j=b)$ thresholds, cf. Table IV. The thresholds are indicated by dashed-dotted lines. Seven lowest $b=4$ levels are also shown in the left panel. All segments in $k \geqslant 1$ columns represent two closely spaced (e,f) levels. In the left panel, e levels between $j=0$ and $j=2$ thresholds and all levels above $j=2$ pertain to resonances of (predominantly) Feshbach type. In the right panel, all levels above $j=1$ threshold pertain to resonances.

TABLE V. Energies of $J \geqslant k$ levels in selected (b,k,v_R,p) states of $HeH_2^+(A)$. $p=-1$ in $k>0$ cases shown. Parameters of the fit to the polynomial listed in Table III. Deperturbed values are given (in the last two lines) for Coriolis coupled $(b=2,k=1,v_R=0)$ and $(b=k=2,v_R=1)$ states. All parameters are in cm^{-1}

b	k	v_R	E^{0a}	B	D 10^4	H 10^6	β^b	$dev^{b,c}$
0	0	0	−817.03	1.98	3.29	−0.06		0.00
		1	*278.61*	1.74	3.86	0.17		0.09
1	0	0	−508.82	1.85	3.83	−0.19		0.00
		1	*222.36*	1.57	5.32	0.32		0.05
1	1	0	−865.07	2.01	3.35	−0.08		0.00
		1	*283.04*	1.76	3.86	−0.81		0.07
2	0	0	−409.49	1.79	7.76	−3.03		0.02
2	2	0	−899.06	1.96	3.10	−0.06		0.00
2	1	0	−619.95	1.88	20.26	−55.03		8.82
2	2	1	−611.18	1.58	−275.63	−937.16		182.0
2	1	0	−614.25	1.91	3.76	−0.10	0.30	0.39
2	2	1	−616.67	1.72	3.73	−0.12	0.30	0.39

[a] Given relative to the $He^+ + H_2(v=0,j=b)$ thresholds, see Table IV. Italic numbers are relative to the values in preceding lines (the stretching frequencies).

[b] See Table III.

[c] In the $(b,k,v_R)=(2,0,0)$ case, there are only six bound J levels. *dev* accounts only for these levels.

clear assignment of levels to particular j thresholds is possible which is due to the fact that the anisotropy of the potential is weaker and that the separations between the thresholds are larger. This justifies categorization of the system as a case 2 atom–diatom complex according to the classification given in Ref. 25. Second, levels assigned to a given j threshold (and to a given stretching state) form a descending sequence for k growing from 0 to j, a feature which is known to be common among nonrigid complexes with T-shaped equilibrium geometry.

A direct quantitative comparison of some characteristics of the spectrum of $HeH_2^+(A)$ with their $HeH_2^+(X)$ analogs further demonstrates the basic difference between the two states. From the numbers in Table V for the spectroscopic parameter E^0 a splitting of 365.25 cm^{-1} between $(b,k,v_R) = (1,1,0)$ and (1, 0, 0) states is obtained. Considering this quantity to be a counterpart of the $HeH_2^+(X)$ fundamental bending frequency of 635.80 cm^{-1} (Table III), then the ratio of the two numbers can be viewed as a measure for the smaller anisotropy of the A-state potential. Apart from this, the shallowness and almost long-range binding character (large R_e value) of the A-state potential lead to substantial differences in the spectroscopic parameters such as much smaller stretching frequencies and rotational constants B as listed in Table V. Finally, the values of the parameter β in Tables III and V show that the strength of the Coriolis coupling in the A state is much smaller compared to the ground electronic state.

C. Quasibound states of $HeH_2^+(A)$

The ranges of continuum energy E which are important for the association of He^+ with $H_2(I)$ at temperatures below 100 K can be estimated as extending up to 300 cm^{-1} above the thresholds $He^+ + H_2(v=0,j=I)$ at $E = 0$ cm^{-1} and $E = 118.20$ cm^{-1} for $I=0$ and $I=1$, respectively. These ranges were searched for nonbroad ($\Gamma < 1$ cm^{-1}) resonances with $J \leqslant 21$ and $J \leqslant 22$ for $I=0$ and $I=1$, respectively. Altogether 198 such resonances are found; 115 of them are quasibound

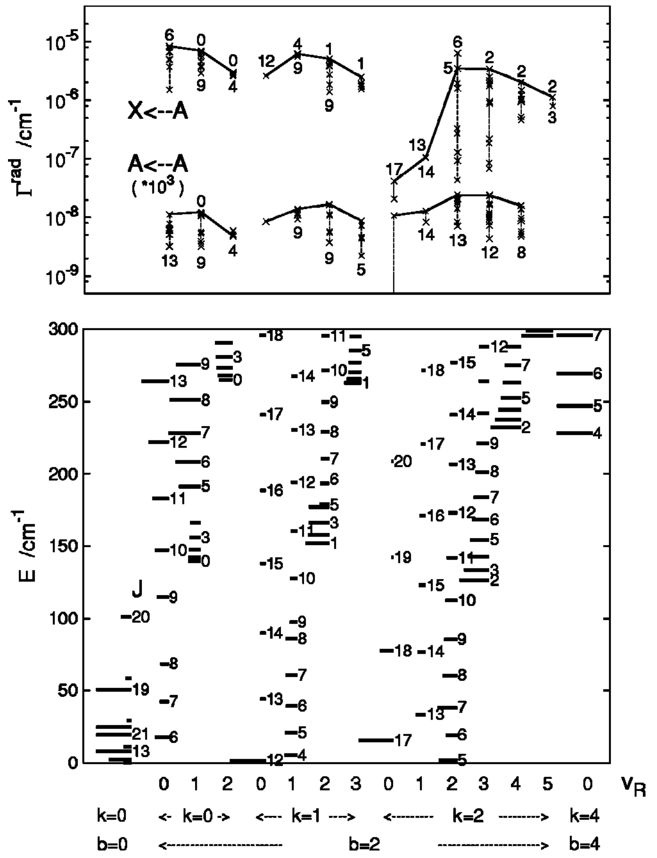

FIG. 4. Quasibound states of $HeH_2^+(A;I=0)$ in the range up to 300 cm^{-1} above the $He^+ + H_2(v=0,j=0)$ threshold, cf. Fig. 3. Lower panel: Energies and dissociative widths of the states. Shown are only states characterized by $\Gamma < 1$ cm^{-1}. The widths are indicated by lengths of the segments; the lengths are proportional to $|\log \Gamma|$ if $\Gamma > 10^{-5}$ cm^{-1}. The longest segments represent widths $\Gamma \leqslant 10^{-5}$ cm^{-1}. Full assignment is shown of all states except for the ones in the leftmost column (see Table VI for v_R and J numbers of these states). Upper panel: Radiative widths of sharp ($\Gamma \leqslant 0.1$ cm^{-1}) resonances associated with the $j=2$ threshold. The widths pertaining to $A \leftarrow A$ process are multiplied by 10^3. Crosses representing widths of the lowest-energy states from particular (k,v_R) groups are joined with solid lines.

TABLE VI. Energies and widths, dissociative and radiative (all in cm^{-1}), of the most important A-state resonances ($I=0, p=1$). Maximal contributions of the resonances to the rate constant $k(X \leftarrow A)$ as a function of temperature is shown (in $s^{-1}\,cm^3$) behind the vertical line (T_{max} in K).

k	$[v]$	$(b v_R)$	%[a]	J	E^{res}	Γ	Γ^{rad}			
							$A \leftarrow A$ $\times 10^{11}$	$X \leftarrow A \times 10^6$	T_{max}	$k^{res}(T_{max})$ $X \leftarrow A \times 10^{16}$
0	9	(0 7)		3	0.32	9.7(−2)	[b]			
	9			4	0.9	0.9				
	8	(0 6)		6	1.7	0.1				
	7	(0 5)	97	8	2.16	0.7(−3)	0.20			
	5	(0 4)		11	11.1	0.1				
	4	(0 3)	96	13	7.96	1.2(−7)	0.67	0.08	7.6	0.08
	4			14	28.0	2.7(−1)				
	3	(0 2)	98	16	24.65	3.6(−6)	0.90	0.01	23	0.00
	3			17	58.5	0.2				
	2	(0 1)	98	19	50.69	2.3(−6)	1.27	0.00		
	1	(0 0)	99	21	19.72	~ 0[c]	1.84	0.00		
	6	(2 0)	57	6	17.61	1.2(−2)	1.13	8.34	17	2.25
	6		77	7	42.19	5.8(−2)	0.66	7.79	34	0.60
	6		71	8	68.51	7.7(−2)	0.62	6.60	46	0.22
1	2	(2 1)	89	4	5.25	1.7(−2)	1.38	6.18	5.0	7.08
	2		86	5	20.66	2.4(−2)	1.32	6.13	20	1.10
	2		84	6	39.18	3.0(−2)	1.30	6.22	32	0.47
	2		75	7	60.89	3.2(−2)	1.18	6.23	42	0.24
	2		70	8	85.95	3.0(−2)	1.09	5.52	53	0.11
	2			9	97.2	0.1				
	1	(2 0)	61	12	1.54	~ 0[c]	0.85	2.61		
	1			13	44.2	0.2				
	1			14	89.8	0.2				
2	3	(2 2)	94	5	1.68	2.7(−3)	2.45	3.48	1.6	26.55
	3		65	6	19.23	3.1(−2)	1.76	6.36	18.0	1.50
	3		85	7	38.12	1.8(−3)	2.08	1.95	32	0.18
	3		90	8	60.50	8.4(−3)	2.04	1.61	42	0.07
	3		91	9	85.34	1.7(−2)	1.90	0.33	52	0.01
	2	(2 1)	72	13	33.26	4.7(−2)	1.28	0.11	29	0.02
	2		74	14	76.92	8.9(−2)	0.83	0.10	49	0.00
	1	(2 0)	93	17	15.52	~ 0[c]	1.07	0.04		
	1		90	18	77.55	1.3(−02)	0.00	0.02	49	0.00

[a] Occupancy of the configuration ($v_r=0, k, b, v_R$) in the natural expansion of function of the state, see Table VII. In the cases shown, the occupancy is at most smaller by 2% than the corresponding value of $\rho_{\lambda=k}$; no mixing of vibrational (r, θ, R) modes practically occurs within the $\lambda=k$ component of the function.

[b] An empty entry in Γ^{rad} column means that the resonance was included in the background part of the rate constant for the process indicated.

[c] The width is much smaller than Γ^{tot}, see Eq. (15) and Sec. IV D

states of $HeH_2^+(A; I=0)$. Energies of these states, the quantum numbers b, k, v_R, and J assigned to them, and the dissociative widths Γ are shown in the lower panel of Fig. 4. The widths Γ of most of the resonances (80 and 51 for $I=0$ and $I=1$, respectively) are found to be smaller than 0.1 cm^{-1}. They are treated as sharp resonances in the calculations of the rate constants of reactions (2) and (3) and their radiative widths Γ^{rad} are evaluated using Eq. (14). The magnitudes of the radiative widths and some correlations with the assignments of the resonances are displayed in the upper panel of Fig. 4. In Table VI, the characteristics determined of all 32 A-state resonances in the range below 100 cm^{-1} are listed, such as their positions E^{res}, the widths Γ, $\Gamma^{rad}(A \leftarrow A)$ and $\Gamma^{rad}(X \leftarrow A)$, as well as their complete labeling with the numbers k, b, v_R, and J ($p=1$ and $v_r=0$ in all cases). Also maximal contributions of the sharp resonances to the rate constant $k(T)$ of $X \leftarrow A$ process are estimated. For comparison, analogous information is provided in Table VII on selected X-state resonances extending partly the information available previously in paper I. Tendencies among rates $\frac{1}{\hbar}\Gamma_{\mathcal{B}}^{rad}$ of individual bound←resonance transitions in reactions (2) and (3) are illustrated in Fig. 5. More details on the transitions in the $X \leftarrow A$ process are presented in Table VIII. In particular, the two main factors that determine $\Gamma_{\mathcal{B}}^{rad}$ according to Eq. (14) are listed: the transition line strength $|T(\mathcal{B};\mathcal{R})|^2$ and the transition energy factor $(E^{res}-E^{B})^3$, called hereafter $\mathcal{S}$- and $\mathcal{E}$ factor, respectively. Figure 6 provides an illustration to the discussion of the $\mathcal{S}$ factors showing probability densities which characterize the spatial extent in R- and θ coordinates of terminal states in three representative $\mathcal{B}(X) \leftarrow \mathcal{R}(A)$ transitions. Information on selected $\mathcal{B} \leftarrow \mathcal{R}$ transitions in the $A \leftarrow A$ and $X \leftarrow X$ processes, analogous to that in Table VIII, is given in Table IX.

The energy-level patterns plotted in Fig. 4 are essentially consistent with what one would expect from the characterization of the bound-state spectrum of $HeH_2^+(A)$ given in Sec.

TABLE VII. Selected X-state resonances ($I=0,p=1$). Shown are energies E^{res}, widths Γ and Γ^{rad} (all cm^{-1}), maximal contributions $k_{\max}=k^{\mathrm{res}}(T_{\max})$ (in s^{-1} cm^3) to rate constant $k(T)$ of $X \leftarrow X$ process ($T_{\max}$ in K), and results of the natural expansion analysis (NEA) of resonance functions. [Analyzed were bound-state functions approximating the quasibound ones. The approximation is rather crude in cases with $\Gamma > 0.1$ cm^{-1}. Therefore the occupancies (column 10) of the leading natural configurations (column 9) have only qualitative meaning in these cases].

k^{a}	$[v]^{a}$	J	E^{res}	Γ	$\Gamma^{\mathrm{rad}}\times 10^{11}$	$T_{\max}$	$k_{\max}\times 10^{21}$	$(\lambda\, v_\theta v_R)$	%
0	7	8	15.4	3.4(−01)	4.50	14.0	1.88	(0 0 4)	85
	5(6)	11	23.44	2.3(−04)	7.34	18.0	2.02	(0 0 3)	79
	3(4)	14	29.10	2.6(−09)	13.99	20.5	3.01	(0 0 2)	74
	2	18	83.71	4.7(−10)	12.46	46.0	0.06	(0 0 1)	66
								(1 0 1)	18
	4(3)	12	10.46	5.0(−12)	7.73	9.9	0.53	(0 2 1)	45
								(1 0 1)	23
	6(5)	9	14.12	2.1(−03)	4.91	13.0	2.66	(0 0 3)	56
								(0 2 1)	17
								(1 0 2)	16
1	3	9	27.4	5.5(−01)	4.83	20.0	0.81	(0 0 2)	35
								(0 2 4)	14
								(1 0 1)	36
2	2	8	29.59	8.4(−03)	2.13	20.7	0.27	(2 0 1)	77
	3	2	15.92	2.9(−03)	4.87	14.0	0.57	(2 0 2)	73

[a]These are the labels assigned to the states in Ref. 1 by inspecting solely the progressions of energies of bound and quasibound states. In parentheses are the most obvious changes indicated by NEA of functions of the states; compare columns 9 and 10 with Table II.

III B. There are only a few $b=0$ states whereas the majority of states are the rotationally predissociating $b=2$ states. Coriolis coupling appears to cause the exchange of $J \geqslant 9$ levels between the (2, 0, 0) and (2, 1, 1) states and similarly of $J \geqslant 6$ levels between the (2, 0, 1) and (2, 1, 2) states. It also affects the dissociative widths as can be seen from the nonuniform variation of the widths of the ($b=2,k=0,v_R=0$, 1) states with increasing J. Actually, all the predissociation widths are a combined effect of the potential anisotropy and the Coriolis interaction. A more detailed, perturbative analysis of these widths will be presented in a future publication.

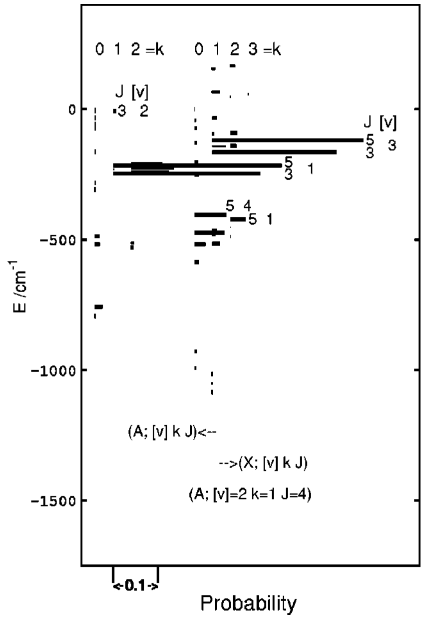

FIG. 5. Probabilities $\Gamma^{\mathrm{rad}}_{\mathcal{B}}/\Gamma^{\mathrm{rad}}$ of stabilization of a representative quasibound state of $\mathrm{HeH}_2^+(A)$, $\mathcal{R}=(I=0,[v]=2,k=1,J=4,p=1)$ (cf. Table VI), in different bound states $\mathcal{B}=(I=0,[v],k,J=3-5)$ of $\mathrm{HeH}_2^+(X)$ and $\mathrm{HeH}_2^+(A)$. Energies of $\mathcal{B}$ states are shown relative to the dissociation threshold of their respective electronic state. The probabilities of stabilization of $\mathcal{R}$ in all (17 and 14) states $(X;k)$ with $k=0$ and $k=1$, and in (3) states $(X;[v]=3,k=1)$ are 21.6%, 70.9%, and 64%, respectively. The stabilization probabilities in (4 and 8) states $(A;k)$ with $k=1$ and $k=2$, and in (3) states $(A;[v]=1,k=1)$ are, respectively, 70.7%, 25.4%, and 70%. Note the big difference between the probabilities of transitions to $(A;[v]=2,k=1,J=3)$ state and to $[v]=1,J=3$, 5 states. The relatively largest $\mathcal{S}$ factor of the first transition, preserving $[v]$ numbers, is damped by its small $\mathcal{E}$ factor, cf. Table IX.

The present discussion concentrates on the radiative widths of the quasibound $\mathrm{HeH}_2^+(A;I=0)$ states. For most of them $\Gamma^{\mathrm{rad}}(X \leftarrow A)$ is in the range of 10^{-6}–10^{-5} cm^{-1}, with the maximum value of 8.34×10^{-6} cm^{-1} for the $(b,k,v_R,J)=(2,0,0,6)$ state. Looking at the $\Gamma^{\mathrm{rad}}(X \leftarrow A)$ results in Table VI and Fig. 4 one notices that

(i) the widths of the $b=0$ states are at least two orders of magnitude smaller than the widths of the $b=2$ states,
(ii) $b=0$ widths decrease rapidly with increasing J,
(iii) for $b=2$ the change of the widths with increasing (v_R,J) is relatively small for states with $k=0$, 1 but becomes considerably larger among $b=k=2$ states. The largest $k=2$ widths are smaller than $k=0$ widths.

In contrast, the $\Gamma^{\mathrm{rad}}(A \leftarrow A)$ results are about five orders of magnitude smaller and their correlation with the quantum numbers differs entirely from the three items specified above for $X \leftarrow A$ transitions. First, the $\Gamma^{\mathrm{rad}}(A \leftarrow A)$ widths of $b=0$ states are comparable to $b=2$ widths. Second, for $b=0$ the widths increase with J and with decreasing v_R; for example, the value for (0, 0, 0, 21) is nearly three times larger than the value for (0, 0, 3, 13). Finally, among the states $(b=2,k,v_R,J)$ which are close in energy and have similar J values, the largest widths occur for those with $k=2$.

A comparison with X-state resonances is also of interest at this point. The first four examples listed in Table VII, assigned with $k+v_\theta=0$, are clearly shape resonances, counterparts of the $b=0$ quasibound states of $\mathrm{HeH}_2^+(A)$. The other examples may be treated approximately as analogs of the

TABLE VIII. $\mathcal{B}$ound$\leftarrow\mathcal{R}$esonance transitions of largest rates in $X\leftarrow A$ process. For each transition shown are: assignments of terminal states, energy E^{res} of initial state (relative to A state dissociation threshold) and transition energy $E^{\mathrm{res}}-E^{B}+74507\overset{\mathrm{def}}{=}\mathcal{E}^{1/3}$ (both in cm^{-1}), transition line strength $\mathcal{S}\overset{\mathrm{def}}{=}|T(\mathcal{B};\mathcal{R})|^2$ (in Debye^2), and $\Gamma^{\mathrm{rad}}_{\mathcal{B}}$ in (cm^{-1}). [$\Gamma^{\mathrm{rad}}_{\mathcal{B}}$ (cm^{-1})$/5.3088\times10^{-12}$ gives rate in s^{-1}.] Behind the vertical line listed are: contribution of the transition to total radiative width of $\mathcal{R}$ and total number of transitions contributing to Γ^{rad}.

$\mathcal{B}$[a]			$\mathcal{R}$									
$[v]$	k	J	b	k	v_R	J	E^{res}	$\mathcal{E}^{1/3}-74\,507$	$\mathcal{S}\times10^3$	$\Gamma^{\mathrm{rad}}_{\mathcal{B}}\times10^6$	$\Gamma^{\mathrm{rad}}_{\mathcal{B}}/\Gamma^{\mathrm{rad}}\times100\%$	N_{trn}
7	0	1	2	0	1	0	139.57	233.41	3.37	2.34	33.5	13
6	0	6	2	0	0	7	42.19	141.47	3.26	2.26	29.0	30
4	0	1	2	0	1	0	139.57	650.38	3.00	2.12	30.3	13
3	1	5	2	1	1	4[b]	5.25	125.03	2.98	2.06	33.4[c]	41
3	1	6	2	1	1	5	20.66	110.82	2.73	1.88	30.8	37
6	0	5[b]	2	0	0	6[b]	17.61	146.87	2.58	1.79	21.4	33
2[d]	2	6	2	2	2	5[b]	1.68	57.65	2.02	1.40	40.1	37
4[e]	0	12	0	0	3	13	7.96	121.13	0.05	0.03	46.0	8

[a] Correlations of $[v]$ with (v_θ,v_R) are as shown in Table II.

[b] See Fig. 5 for full probability distribution in this case, among 41 states $\mathcal{B}=(X;[v],k,J=3-5)$.

[c] See Fig. 6 for probability density $\rho_{\lambda=k}(R,\theta)$ pertaining to the state.

[d] Shown as representative of transitions from $(b,k,v_R)=(2,2,2)$ resonances.

[e] Shown as transition from shape resonance of largest strength.

predissociating $b=2$ states (although the analogy cannot be strict because of the sizable $\theta-R$ mode mixing, as shown in the last two columns). The radiative widths of the X-state resonances, as describing a single-state process, are much closer to the widths $\Gamma^{\mathrm{rad}}(A\leftarrow A)$ than to $\Gamma^{\mathrm{rad}}(X\leftarrow A)$. The widths $\Gamma^{\mathrm{rad}}(X\leftarrow X)$ are only slightly larger than the widths $\Gamma^{\mathrm{rad}}(X\leftarrow A)$. Also, no clear cutoff is seen between the values for $k+v_\theta=0$ and for $k+v_\theta>0$ resonances. However, there are also some noticeable differences between the radiative widths of the resonances in $X\leftarrow X$ and $A\leftarrow A$ processes. Namely, the largest $\Gamma^{\mathrm{rad}}(X\leftarrow X)$ pertain to shape resonances. These widths do not behave as monotonically with decreasing v_R as the widths $\Gamma^{\mathrm{rad}}(A\leftarrow A)$ of $b=0$ states.

In order to rationalize the above observations, it is necessary to examine the partial widths $\Gamma^{\mathrm{rad}}_{\mathcal{B}}$ of the resonances. Two examples in Fig. 5 for the probability distributions $\Gamma^{\mathrm{rad}}_{\mathcal{B}}/\Gamma^{\mathrm{rad}}$ illustrate that there is a considerable selectivity among R-, P-, and Q transitions to the different states $\mathcal{B}=(X;[v],k,J)$ or $\mathcal{B}=(A;[v],k,J)$ which can stabilize a given resonance $\mathcal{R}=(A;[v],k,J)$. In both transitions $A\leftarrow A$ and $X\leftarrow A$ a strong propensity is observed preserving the number k (which also exists in $X\leftarrow X$ transitions). The propensity is due to the properties of the dipole vector operators used,[1,16] i.e., nonvanishing dipole transition amplitudes can only arise between components of the states with the same λ value. Transitions changing k are thus only possible if Coriolis mix-

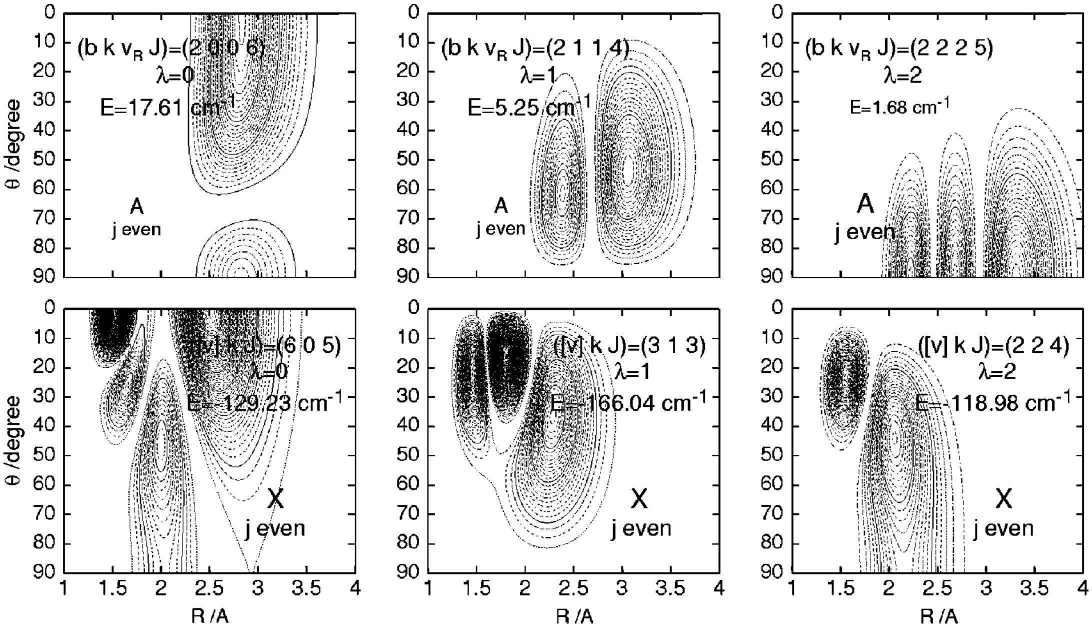

FIG. 6. Probability densities $\rho_\lambda(EJp;R,\theta)=\int r^2dr|\Psi_\lambda(E,J,p;r,R,\theta)|^2$ for the largest λ components of terminal states in three representative bound $\leftarrow$resonance transitions in $X\leftarrow A$ process, cf. Table VIII. Making use of symmetry $\Psi_\lambda(\cdots\pi-\theta)=(-)^{I+\lambda}\Psi_\lambda(\cdots\theta)$, the densities are shown only in half of the range of θ. The contours are shown with a step of 0.05. The integrated values ρ_λ are 0.59, 0.92, and 0.97 for the upper states (cf. Table VI), and 0.88, 0.90, and 0.89 for the lower states.

TABLE IX. Selected bound←resonance transitions in $A\leftarrow A$ and $X\leftarrow X$ processes. All quantities are as in Table VIII.

$\mathcal{B}$				$\mathcal{R}$									
b	k	υ_R	J	b	k	υ_R	J	E^{res}	$\mathcal{E}^{1/3}$	$\mathcal{S}$	$\Gamma_{\mathcal{B}}^{\mathrm{rad}}\times 10^{11}$	$\Gamma_{\mathcal{B}}^{\mathrm{rad}}/\Gamma^{\mathrm{rad}}\times 100\%$	N_{trn}
0	0	0	20	0	0	0	21	19.72	68.35	3.45(+1)	1.858	100	1
0	0	1	18	0	0	1	19	50.69	50.91	4.51(+1)	0.990	77.8	3
0	0	2	15	0	0	2	16	24.65	35.00	5.86(+1)	0.418	46.7	7
0	0	1	14	0	0	3	13	7.96	201.32	0.11(+0)	0.145	21.8	11
^{a}0	0	3	12						22.29	7.82(+1)		21.7	
2	2	1	6	2	2	2	5	1.68	193.10	5.03(−1)	0.604	24.7	24
^{a}2	2	2	4						14.34	3.28(+1)		0.7	
2	1	0	5	2	1	1	4	5.25	221.43	2.86(−1)	0.517	37.4^{b}	28
^{a}2	1	1	3						12.31	3.02(+1)		0.7^{b}	
^{c}2	1	0	9	2	2	2	8^{d}	60.50	175.78	6.71(−1)	0.607	29.8	20
^{c}2	2	1	8	2	0	0	7	42.19	182.09	2.02(−1)	0.203	31.0	20
2	0	0	1	2	0	1	0	139.52	191.41	7.58(−1)	0.886	72.0	11
2	2	2	2	2	2	3	2	126.46	159.32	1.18(+0)	0.793	32.7	29
	$[\upsilon]^{e}$	k	J		$[\upsilon]^{e}$	k	J						
	1	0	20		1	0	21	31.72	154.98	8.96(+0)	5.55	100	1
	1	0	17		2	0	18	83.71	636.84	1.65(−1)	7.09	56.7	3
	^{a}2	0	17						114.88	1.27(+1)		25.7	
	1	0	13		4	0	14	29.10	1063.46	2.04(−2)	4.09	29.3	8
	^{a}4	0	13						72.64	1.92(+1)		8.8	
	1	1	10		6	0	11	23.44	734.54	2.37(−2)	1.56	21.3	16
	^{a}6	0	10						42.36	3.03(+1)		5.2	
	^{f}1	0	10						1343.16	2.90(−3)		15.9	

[a] Transition from $\mathcal{R}$ characterized by the largest $\mathcal{S}$ factor, shown only when it does not coincide with the transition in the upper line, giving the largest $\Gamma_{\mathcal{B}}^{\mathrm{rad}}\sim\mathcal{E}\mathcal{S}$.

[b] Probability distribution among all N_{trn} states $\mathcal{B}=(A;b,k,\upsilon_R,J)$ is shown in Fig. 5. Note that (b,k,υ_R) corresponds to $([\upsilon]=\upsilon_R+1,k)$ for $b=2$, $k=1$, 2 and for $b=k=0$, $\upsilon_R\leqslant 4$, cf. Table IV.

[c] Example of transition changing k number. See Table VI for information on λ mixing in $\mathcal{R}$ state. A mixing of similar degree, between $\lambda=2$ and $\lambda=1$ components, occurs in $\mathcal{B}$ state.

[d] This resonance and the three following examples cannot be stabilized by pure rotational transitions.

[e] $[\upsilon]=1$, 2, 4, 6 correlate with $\upsilon_\theta=0$, $\upsilon_R=0$, 1, 2, 3, cf. Table II.

[f] Transition with $\Delta\upsilon_R=3$; striking example of the role of $\mathcal{E}$ factor in determining $\Gamma_{\mathcal{B}}^{\mathrm{rad}}/\Gamma^{\mathrm{rad}}$.

ing of different λ components in terminal states takes place. An even stronger selectivity in $\mathcal{B}\leftarrow\mathcal{R}$ transitions is associated with $[\upsilon]$ numbers of the states, cf. the caption of Fig. 5. This selectivity is different in the three processes considered. The main difference shows up in the transition energy contribution to the rates $\frac{1}{\hbar}\Gamma_{\mathcal{B}}^{\mathrm{rad}}$. In $X\leftarrow A$ these $\mathcal{E}$ factors are big and practically constant, cf. Table VIII. So, they determine the overall magnitude of the rates but hardly influence any relations between them which are almost completely determined by the $\mathcal{S}$ factors. In the single-state processes, the $\mathcal{E}$ factors vary by several orders of magnitude and contribute to relative rates of $\mathcal{B}\leftarrow\mathcal{R}$ transitions as significantly as the $\mathcal{S}$ factors, cf. Table IX and the last paragraph of this subsection.

The $\mathcal{S}$ factors reflect the overlapping between resonance and bound-state functions, or rather between their respective λ components. There are obviously correlations between this overlapping of the functions and $[\upsilon]$ numbers assigned to them. In $X\leftarrow A$ these correlations are quite different from those in single-state processes (1) and (3) because of the large geometry rearrangement associated with $X\leftarrow A$ transitions, particularly the big changes in the equilibrium values of the two atom–diatom coordinates, $\Delta R_{\mathrm{e}}=0.775$ Å and $\Delta\theta_{\mathrm{e}}=90°$. Due to the large geometry change the ground vibrational state functions of the initial and product ions, $\mathcal{R}=(A;b=0,k=0,\upsilon_R=0,J)$ and $\mathcal{B}=(X;\upsilon_\theta=0,k=0,\upsilon_R^B=0,J^B)$, overlap very little. But excitations in the R mode of $\mathcal{B}$ states reduce effectively the displacement ΔR_{e}. With growing υ_R^B, the respective functions extend to increasingly larger R distances and therefore the chances to overlap with functions of $\mathcal{R}$ states increase. It should be noted here that only ground vibrational $\mathcal{B}$ states exist with J^B high enough to be reached in transitions from $\mathcal{R}$ states characterized by $J=21-19$. Transitions to vibrationally excited states with $\upsilon_R^B=2$ and $\upsilon_R^B=3$ become possible for resonances with $J\leqslant 14$ and $J\leqslant 12$, respectively. This explains the observation in item (ii) listed above. The majority of $\mathcal{R}$ states with excited bending mode and energies in the range of interest here are characterized by $J<12$, cf. Fig. 4. Thus, $\mathcal{B}$ states of the most delocalized functions (largest υ_R^B, large $\theta-R$ mode mixing) can be reached in $(k,J\pm 1)\leftarrow(k,J)$ transitions from $(b=2,k=0,1,2,\upsilon_R,J<12)$ resonances. In addition to that, a considerable shift towards $\theta=0$, 180° localizations takes place in the $(b=2,k=0,1)$ resonances, cf. Fig. 6. Both displacements ΔR_{e} and $\Delta\theta_{\mathrm{e}}$ are thus compensated. This causes the large increase of $\mathcal{S}$ factors of transitions from $b=2$ resonances compared to transitions from $b=0$ resonances (cf. Table VIII) and explains observation (i). Figure 6 shows also that the overlap conditions for $b=2$ resonances deteriorate slightly when k increases from 0 to 2, observation (iii).

In the $A\leftarrow A$ and $X\leftarrow X$ processes, the largest $\mathcal{S}$ factors pertain to transitions which preserve all vibrational numbers $[v]$ of the initial state (in addition to k, of course). They are P transitions from the lowest J resonances $(J>k)$ atop the particular $([v],k)$ groups of bound states on the respective PES. Table IX shows the increase (with v_R) of the factors $\mathcal{S}(\Delta[v]=0)$ of $(0,0,v_R,J-1)\leftarrow(b=0,k=0,v_R,J)$ transitions in $A\leftarrow A$ and $X\leftarrow X$ processes. The increase reflects mostly the R dependence of the dipole moment vector fields of A- and X states.[16] The values of $\mathcal{S}(\Delta[v]=0)$ for $(b=2,k,v_R,J)$ resonances are smaller but remain within the same order of magnitude as the values for $b=0$ resonances. Most of the $\mathcal{B}\leftarrow\mathcal{R}$ transitions in the processes change the vibrational numbers, especially v_R. Changes of b or v_θ (in $X\leftarrow X$) occur in transitions from $b=2$ or $v_\theta=2$ states labeled with $k=0$. From $k>0$ states, such transitions are possible only because there are admixtures of $\lambda=0$ component. $\mathcal{S}$ factors of $\Delta[v]\neq 0$ transitions are distinctly smaller than the factors of $\Delta[v]=0$ transitions. For $\Delta b=2$ transitions they are very small, comparable to $\mathcal{S}(\Delta v_R=3)$. In general, the decrease of the transition strengths with growing Δv_R or $\Delta b(\Delta v_\theta)$ is slightly faster in $A\leftarrow A$ than in $X\leftarrow X$.

Finally, some details on the role of $\mathcal{E}$ factors of $\mathcal{B}\leftarrow\mathcal{R}$ in the single-state processes are added. In $\Delta[v]=0$ transitions, the factors depend on the amount of the released rotational energy, $\mathcal{E}=(2BJ)^3$. $\mathcal{E}$ factors of transitions changing v_R increase approximately like $(\Delta E^0)^3$. Thus, even the largest factors $\mathcal{E}(\Delta[v]=0)$, pertaining to transitions from resonances with large J, are significantly smaller than the factors of possible $\Delta v_R>0$ transitions from the same resonances. Obviously, the difference between $\mathcal{E}$ factors of pure rotational and (ro)vibrational transitions becomes larger when J is decreasing and Δv_R is increasing (more in $X\leftarrow X$ due to the larger $\Delta E^0/B$ than in $A\leftarrow A$). The dominance of $\mathcal{E}(\Delta v_R>0)$ over $\mathcal{E}(\Delta[v]=0)$ in $X\leftarrow X$ transitions is so big that it always overrides the relations between $\mathcal{S}$ factors of transitions. Despite their large strengths, the purely rotational transitions contribute much smaller amounts to the total widths $\Gamma^{\text{rad}}(X\leftarrow X)$ than the vibrational transitions (see examples in Table IX). In the $A\leftarrow A$ process, the $\mathcal{E}$ factors have generally smaller impact on the probability distributions $\Gamma^{\text{rad}}_{\mathcal{B}}/\Gamma^{\text{rad}}$ among $\mathcal{B}$ states available for a given $\mathcal{R}$ state. This is most clearly seen in the cases of high-J shape resonances (compare the first four cases in Table IX with their X-state counterparts in the lower part of the table). The purely rotational transitions from $J=19$, 16 resonances dominate over the vibrational transitions not only in their strengths ($\mathcal{S}$) but also in their rates ($\sim\mathcal{S}\mathcal{E}$).

D. Rate constants and emission spectra

The resonance parts of $k(T)$ and $\mathcal{I}(\nu,T)$ for the $X\leftarrow A$ and $A\leftarrow A$ processes, including contributions from the sharp A-state resonances mentioned above, are evaluated according to Eqs. (15) and (16). The factors $\Gamma/\Gamma^{\text{tot}}$, "cutting" the sharpest resonances, are used in the same form for both processes, with $\Gamma^{\text{tot}}=\Gamma+\Gamma^{\text{rad}}(X\leftarrow A)+\Gamma^{\text{rad}}(A\leftarrow A)$. Resonances with widths Γ larger than 0.1 cm^{-1} are included in the background contributions to the above quantities. For these background parts, the transition amplitudes $T^I_{vjl}(E^BJ^Bp^B;EJp)$ are evaluated at appropriate energy grid points which covers the ranges 0-300 and $118.20-300$ cm^{-1} for $I=0$ and $I=1$, respectively. In these ranges, the possible initial v, j, l states are $v=0$, $j=0$, $l=J(p=1)$ for $I=0$, and $j=1$, $l=J\pm1(p=1)$, $l=J(p=-1)$ for $I=1$. All possible $J^Bp^B\leftarrow Jp$ transitions in $X\leftarrow A$ and $A\leftarrow A$ processes are counted in Table I(B). Among the total number $1556+1866$ of these transitions, nearly one-third could be omitted in the calculations, mainly because continuum $p=-1$ parity states of He$^+$+H$_2(I=0)$ are negligibly populated at temperatures below 100 K.

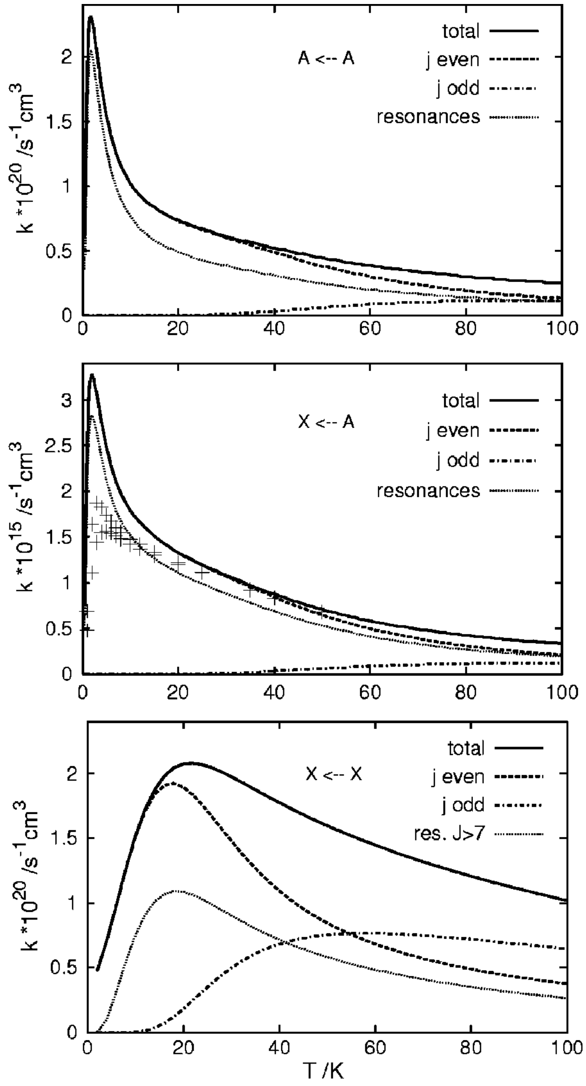

FIG. 7. Rate constants k of $A\leftarrow A$, $X\leftarrow A$, and $X\leftarrow X$ processes at temperatures below 100 K. Shown are also the resolutions $k=k^0+k^1$ and $k\approx k^{\text{res}}+k^{\text{back}}$. The crosses denote results of calculations in which the five lowest lying $b=2$ resonances (cf. Table VI), at $E^{\text{res}}=1.7$, 5.2, 17.6, 19.2, and 20.7 cm^{-1}, were shifted down (upper crosses) or up by 2 cm^{-1}.

Results of calculations performed in this work and those obtained previously in paper I on the temperature-averaged characteristics of RA processes $X\leftarrow A$, $A\leftarrow A$, and $X\leftarrow X$ are presented in Figs. 7–10 and in Table X. In the three panels of Fig. 7 the rate constant functions $k(T)$ of these processes are shown for the temperature range of 1-100 K together with their para- and orthocomponents and the contributions from (sharp) resonances. The corresponding emission intensity functions $\mathcal{I}(T)$ are plotted in Fig. 8. Figure 9 compares at a selected temperature of $T=20$ K the partial rates $k^0_{([v],k)}$

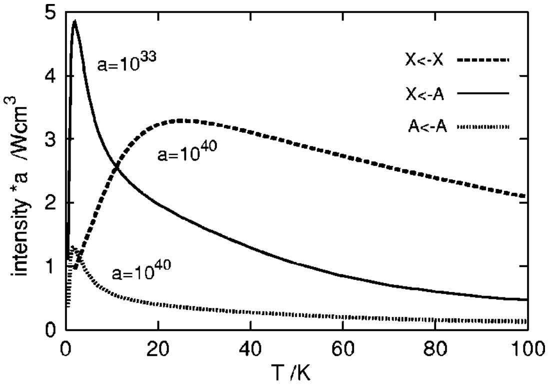

FIG. 8. Intensities $\mathcal{I}(T)$ of photon emission in $A\leftarrow A$, $X\leftarrow A$, and $X\leftarrow X$ processes at temperatures below 100 K.

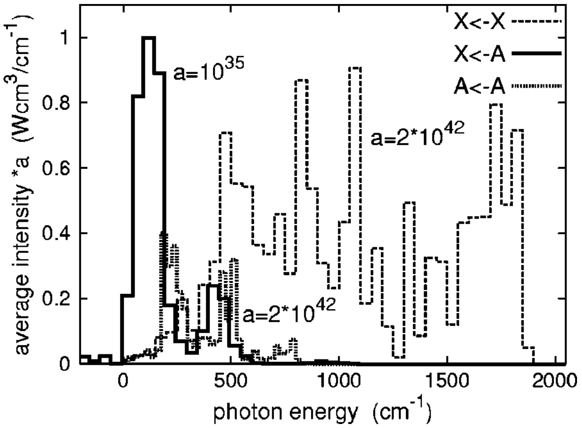

FIG. 10. Emission spectra of $X\leftarrow A$, $A\leftarrow A$, and $X\leftarrow X$ processes at $T=20$ K. Plotted are the average spectrum densities $\overline{\mathcal{I}}(\overline{\nu},\Delta\nu;T)=\frac{1}{\Delta\nu}\int_{\overline{\nu}}^{\overline{\nu}+\Delta\nu}\mathcal{I}(\nu,T)d\nu$, with $\Delta\nu=50$ cm^{-1} for $X\leftarrow A$ and $X\leftarrow X$ and $\Delta\nu=25$ cm^{-1} for $A\leftarrow A$. The corresponding integrated intensities $\mathcal{I}(T=20\text{K})$ are 2.0×10^{-33}, 4.0×10^{-41}, and 3.2×10^{-40} W cm^3, see Fig. 8. Photon energy in the $X\leftarrow A$ process is shown relative to the energy separation between the A- and X-state dissociation thresholds which is 74 507 cm^{-1}.

$\overset{\text{def}}{=}\Sigma_{\mathcal{B}\in([v],k)}k^0_{\mathcal{B}}$ for the formation of the product ions in the rovibrational states belonging to a given group $(I=0,[v],k)$ and in Fig. 10 for the same temperature the spectra of photons emitted in the three processes are compared. Table X finally summarizes in numerical form the results of the present $k(X\leftarrow A)$ and $k(A\leftarrow A)$ rate constant calculations.

The results display two main differences between the $X\leftarrow A$ process and the two single-state processes, $X\leftarrow X$ and $A\leftarrow A$: First of all Figs. 7 and 8 clearly demonstrate that the temperature functions of the rate constant $k(T)$ and of the emissivity $\mathcal{I}(T)$ are orders of magnitude larger for $X\leftarrow A$ compared to the other two reactions. Further, the population of vibrational states of the product ions and the shape of the emission spectra are totally different. The order of magnitude of $k(T)$ in the considered temperature range is mostly determined by the number and the radiative widths of the resonances in the energy range limited by the Boltzmann factor. If sharp and nonbroad resonances are counted together, their total numbers can be estimated to be comparable in the X- and A states (at least in the energy range up to 175 cm^{-1} above their dissociation thresholds). The radiative widths remain thus the main reason for the difference of five or four orders of magnitude seen in Fig. 7 between the values of k for $X\leftarrow A$ and for the two other processes. The additional two orders of magnitude in the difference between the emission intensities seen in Fig. 8 are essentially due to the fact that the transition energies enter the expression for the intensity to the fourth power. A comparison of the shapes of the functions $\mathcal{I}(T)$ and $k(T)$ shows that they are almost identical for the two-state process and differ for $X\leftarrow X$ and less noticeably for $A\leftarrow A$. This is obviously a manifestation of the role of the $\mathcal{E}$ factors of the radiative widths discussed in Sec. IV C. Turning now to the differences in the vibrational-state populations and the emission spectra, Fig. 9 shows that in the $X\leftarrow A$ process the ion is formed in a few highly excited (most delocalized) vibrational states, such as $([v],k)=(2,2)$, (3,1), (6,0), (5,0). A high maximum in the intensity of photon emission occurs at energies not much larger (by about 100 cm^{-1}) than the energy separation between the A- and X-state dissociation thresholds. Almost no intensity is seen in Fig. 9 in the photon energy region which would correspond to the formation of states localized within the collinear wells of the X-state PES. In the $X\leftarrow X$ process, however, the situation is quite the opposite. The ion is formed preferentially in the low bending and stretching states and therefore almost all the emission intensity is placed in the region above 500 cm^{-1}. Similar to the situation in $X\leftarrow X$ is the vibrational-state distribution of the product ion in $A\leftarrow A$. The states of $HeH_2^+(A)$ lying in the lower part of the A-state potential well are mostly populated. The shift of the maximum population off the lowest state is only a quantitative difference. The population of the excited states drops evidently when they approach the dissociation threshold. This is reflected by the emission spectrum calculated for the $A\leftarrow A$ process where

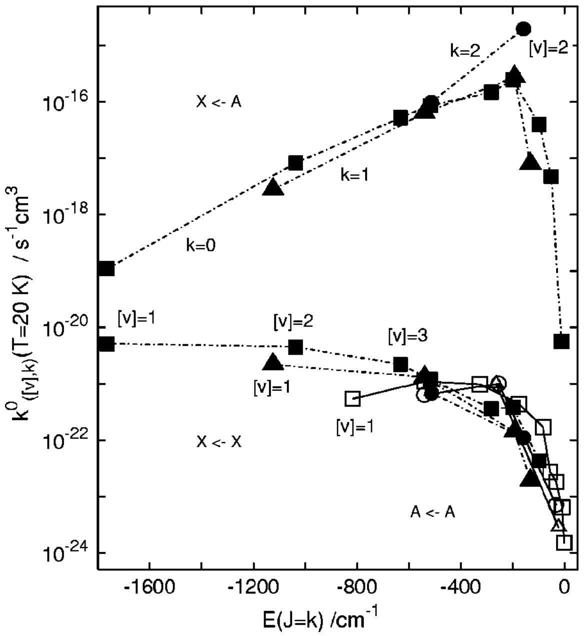

FIG. 9. Partial rate constants $\Sigma_{\mathcal{B}\in([v],k)}k^0_{\mathcal{B}}(T)$ at $T=20$ K for the formation of $HeH_2^+(X)$ and $HeH_2^+(A)$ (open symbols) in different groups $(I=0,[v],k,p=1)$ of rovibrational states, cf. Table I. Squares, triangles, and circles are used for $k=0$, 1, and 2, respectively. Abscissas of the symbols are the energies of $J=k$ states from the groups (relative to the dissociation threshold of the respective electronic state, cf. Tables II and IV.)

TABLE X. Rate constants k for $X \leftarrow A$ and $A \leftarrow A$ processes, in 10^{-15} and in 10^{-20} s^{-1} cm^3, respectively, as functions of temperature T, in K.

$X \leftarrow A$				$A \leftarrow A$			
T	k	T	k	T	k	T	k
1	2.5	16	1.5	1	1.8	16	0.8
2	3.3	18	1.4	2	2.3	18	0.8
3	3.1	20	1.3	3	2.0	20	0.7
4	2.8	25	1.2	4	1.8	25	0.7
5	2.5	30	1.1	5	1.6	30	0.6
6	2.3	40	0.9	6	1.4	40	0.5
7	2.1	50	0.7	7	1.3	50	0.4
8	2.0	60	0.6	8	1.2	60	0.4
9	1.9	70	0.5	9	1.1	70	0.3
10	1.8	80	0.4	10	1.0	80	0.3
12	1.7	90	0.4	12	0.9	90	0.3
14	1.6	100	0.3	14	0.9	100	0.3

the intensity turns to be very small on both sides of the spectrum. The differences discussed here reflect most closely the differences between individual resonance-bound transition rates in the processes discussed in Sec. IV C.

There are other features, however, where the two processes starting from the A state, $X \leftarrow A$ and $A \leftarrow A$, behave similarly but differ from the $X \leftarrow X$ reaction occurring entirely on the X-state potential. Two items are especially discussed here: the contribution of transitions from sharp resonances to the rate constant $k(T)$ and the shape of the $k(T)$ function at low temperatures. The contribution of sharp resonances to $k(T)$ ranges for $X \leftarrow A$ from 86% at the maximum of the rate constant curve around $T=2$ K to 57% at 100 K and for $A \leftarrow A$ it is even larger at the rate constant maximum with 88% dropping to 44% at 100 K. These contributions are sensitive mostly to the attributes of the resonances which depend on the molecular interactions within the initial electronic state. The dissociative widths Γ decide about how many resonances can be separated from the background and how accurately this can be done. There is no major difference between the widths of the X- and A-state shape resonances. The other resonances are, however, definitely broader in the X state which is due to the stronger coupling between the bending and stretching modes. It is stated in Secs. IV A and IV B that the X-state complex belongs to the higher anisotropy class of atom–diatom complexes than the A-state complex. The contributions of low-energy resonances of comparable radiative widths strongly depend on their actual positions. In the range below 20 cm^{-1}, the maximal contributions of resonances to $k(T)$ scale like $(E^{\text{res}})^{-3/2}$, cf. Table VI. Discussing the shape of the $k(T)$ functions at low temperatures, Fig. 7 shows that the $k(X \leftarrow A)$ and $k(A \leftarrow A)$ curves are very similar in this temperature range and have nearly identical sharp maxima at temperatures of ~ 2 K. The shapes of the $k(T)$ functions are extremely sensitive to the positions of the low-energy resonances. The curvature of the peak in the individual function $k_{\mathcal{B} \leftarrow \mathcal{R}}(T)$, cf. Eq. (15), scales like $(E^{\text{res}})^{-7/2}$ (for low E^{res}). The positions of maxima in the functions $k(T)$ for $X \leftarrow A$ and $A \leftarrow A$ are determined by the energy of one resonance $(b,k,v_R,J)=(2,2,2,5)$, at 1.7 cm^{-1}. Four additional resonances (2,1,1,4), (2,0,0,6), (2,1,1,5), and (2,2,2,6) are also very important at low temperatures as it follows from the values for $k^{\text{res}}(T_{\max})$ in Table VI. Together with (2,2,2,5) they make about 90% of the entire resonance contribution to $k(X \leftarrow A)$ at temperatures around 20 K (and 70% at 40 K).

V. FINAL REMARKS

The present calculations and the preceding determinations of electronic energy potentials and dipole moment functions are performed on a highly accurate level ensuring that the accuracy of the radiative widths of the A-state resonances and hence the overall magnitude of $k(T)$ are reasonable. Most uncertain in this context is the shape of the $k(T)$ functions for $X \leftarrow A$ and $A \leftarrow A$ at low temperatures due to the fact that the positions of the resonances just above the dissociation threshold are very sensitive to inaccuracies in the asymptotic regions of the calculated potential surfaces. As pointed out in Ref. 2, the accuracy of the PES for the A state is comparable to that for the X state used in paper I. In the discussion of paper I, near-dissociation vibration-rotation energy levels of the X state were compared to the energies from the potential of Ref. 11. The largest differences were found to be close to 2 cm^{-1}. Using this difference as a maximum inaccuracy measure of the near-threshold A-state energies, test calculations were performed to check how this inaccuracy can possibly influence the rate constant behavior as a function of temperature. The effect on the $X \leftarrow A$ rate constant curve of shifting the five most influential resonances up or down by the 2-cm^{-1} inaccuracy margin is indicated as crosses in the corresponding panel of Fig. 7. The function $k(T)$ in the maximum region is thus lowered considerably, by about 50%. Therefore, in terms of a discussion of the accuracy of the present results, the values provided in Table X for the rate constant below 10 K should be treated with some caution. However, taking the accuracy limitations of experimental rate constant determinations into account, such an uncertainty of the theoretical result does not pose a serious problem. The values of k at higher temperatures (above 10 K) are much less sensitive to small shifts of resonance energies.

The temperatures for which the experimental values of the rate constant of RCT reaction (4) are provided in Ref. 5 range from 15 to 40 K. For these temperatures the values of k obtained in this study for RA reaction (2) are in the range of $(1.5-0.9)\times 10^{-15}\ \mathrm{s}^{-1}\,\mathrm{cm}^{-3}$ which means that they are about 7-10 times smaller than the experimental $k(\mathrm{RCT})$ values. It actually turns out that subtraction of the present $k(\mathrm{RA})$ values from the theoretical values of Kimura and Lane for $k(\mathrm{RCT})+k(\mathrm{RA})$, see Fig. 4 in Ref. 6, would seemingly improve the consistency of theory with experiment. It is an essential point in the discussion presented in Sec. IV to demonstrate that rotationally predissociating states (Feshbach resonances) play an absolutely crucial role in the dynamics of RA reactions (2) and (3) at low temperatures. Almost 100% of the entire resonance contributions to $k(X\leftarrow A)$ come from these states. This is a strong evidence for the fact that resonances of this kind have to be taken into account in modeling RCT reaction (4). This was not possible in Kimura and Lane's model. Therefore, calculations based on a more rigorous model are needed in order to make a reliable theoretical simulation of the experimental results of Schauer *et al.* for $k(\mathrm{RCT})$.

Apart from demonstrating the significance of rotational predissociation in the low-energy dynamics of the radiative processes in $\mathrm{He}^{+}+\mathrm{H}_2$, the present calculations give the first, fairly reliable prediction of the rate constant of the $X\leftarrow A$ RA reaction.

[1] F. Mrugała, V. Špirko, and W. P. Kraemer, J. Chem. Phys. **118**, 10547 (2003).

[2] W. P. Kraemer, V. Špirko, and O. Bludsky, Chem. Phys. **276**, 225 (2002).

[3] M. Juřek, V. Špirko, and W. P. Kraemer, Chem. Phys. **193**, 287 (1995).

[4] W. P. Kraemer, V. Špirko, and M. Juřek, Chem. Phys. Lett. **236**, 177 (1995).

[5] M. M. Schauer, S. R. Jefferts, S. E. Barlow, and G. H. Dunn, J. Chem. Phys. **91**, 4592 (1989).

[6] M. Kimura and N. F. Lane, Phys. Rev. A **44**, 259 (1991).

[7] D. G. Hopper, J. Chem. Phys. **73**, 3289 (1980).

[8] R. J. Furlan, G. Bent, and R. Russek, J. Chem. Phys. **93**, 6676 (1990).

[9] J. Tennyson and S. Miller, J. Chem. Phys. **87**, 6648 (1987).

[10] V. Spirko and W. P. Kraemer, J. Mol. Spectrosc. **172**, 265 (1995).

[11] M. Meuwly and J. M. Hutson, J. Chem. Phys. **110**, 3418 (1999).

[12] B. Maiti and N. Sathyamurphy, Chem. Phys. Lett. **345**, 461 (2001).

[13] B. Zygelman and A. Dalgarno, Astrophys. J. **365**, 239 (1990).

[14] B. Zygelman, A. Dalgarno, M. Kimura, and N. F. Lane, Phys. Rev. A **40**, 2340 (1989).

[15] B. Zygelman, P. C. Stancil, and A. Dalgarno, Astrophys. J. **508**, 151 (1998).

[16] M. Šindelka, V. Špirko, and W. P. Kraemer, Theor. Chem. Acc. **110**, 170 (2003).

[17] F. Mrugała, Int. Rev. Phys. Chem. **12**, 1 (1993).

[18] F. Mrugała and R. Moszynski, J. Chem. Phys. **109**, 10823 (1998).

[19] R. M. Stratt, N. C. Handy, and W. H. Miller, J. Chem. Phys. **71**, 3311 (1979).

[20] N. Moiseyev and R. E. Wyatt, Chem. Phys. Lett. **112**, 396 (1986).

[21] N. Lipkin, N. Moiseyev, and C. Leforestier, J. Chem. Phys. **98**, 1888 (1993).

[22] R. D. Levine, *Quantum Mechanics of Molecular Rate Processes* (Clarendon, Oxford, 1969).

[23] J. F. Babb and A. Dalgarno, Phys. Rev. A **51**, 3021 (1995).

[24] R. A. Bain and J. N. Bardsley, J. Phys. B **5**, 277 (1972).

[25] M. Hutson, Adv. Mol. Vib. Collision Dyn. **1A**, 1–45 (1991).